

JOINT BAYESIAN ESTIMATION OF QUASAR CONTINUA AND THE LYMAN-ALPHA FOREST FLUX PROBABILITY DISTRIBUTION FUNCTION

ANNA-CHRISTINA EILERS^{1,2*}, JOSEPH F. HENNAWI^{1,3}, KHEE-GAN LEE^{1,4}

Draft Version of September 1, 2018

ABSTRACT

We present a new Bayesian algorithm making use of Markov Chain Monte Carlo sampling that allows us to simultaneously estimate the unknown continuum level of each quasar in an ensemble of high-resolution spectra, as well as their common probability distribution function (PDF) for the transmitted Ly α forest flux. This fully automated PDF regulated continuum fitting method models the unknown quasar continuum with a linear Principal Component Analysis (PCA) basis, with the PCA coefficients treated as nuisance parameters. The method allows one to estimate parameters governing the thermal state of the intergalactic medium (IGM), such as the slope of the temperature-density relation $\gamma - 1$, while marginalizing out continuum uncertainties in a fully Bayesian way. Using realistic mock quasar spectra created from a simplified semi-numerical model of the IGM, we show that this method recovers the underlying quasar continua to a precision of $\simeq 7\%$ and $\simeq 10\%$ at $z = 3$ and $z = 5$, respectively. Given the number of principal component spectra, this is comparable to the underlying accuracy of the PCA model itself. Most importantly, we show that we can achieve a nearly unbiased estimate of the slope $\gamma - 1$ of the IGM temperature-density relation with a precision of $\pm 8.6\%$ at $z = 3$, $\pm 6.1\%$ at $z = 5$, for an ensemble of ten mock high-resolution quasar spectra. Applying this method to real quasar spectra and comparing to a more realistic IGM model from hydrodynamical simulations would enable precise measurements of the thermal and cosmological parameters governing the IGM, albeit with somewhat larger uncertainties given the increased flexibility of the model.

Subject headings: — intergalactic medium — methods: data analysis — quasars: absorption lines

1. INTRODUCTION

The imprint of Lyman- α (Ly α) forest absorption lines observed on the spectra of distant quasars, caused by residual neutral hydrogen along the line of sight in a mostly ionized intergalactic medium (IGM), has become an important tool for constraining cosmology and the IGM at high redshift $2 \lesssim z \lesssim 6$ (see e.g. Croft et al. 1998; Weinberg et al. 2003; Zaldarriaga et al. 2003; Meiksin 2009; Becker et al. 2015; Mortlock 2015; McQuinn 2015). The observed absorption pattern traces density fluctuations of the IGM along the filamentary structure of the cosmic web that arise due to gravitational instability in an universe dominated by cold dark matter (see e.g. Cen et al. 1994; Miralda-Escudé et al. 1996; Davé et al. 1999).

An important characteristic of the fluctuating IGM is a tight relationship between the temperature T and the density contrast Δ of the cosmic gas (Hui & Gnedin 1997; McQuinn & Upton Sanderbeck 2015). This ‘equation of state’ is controlled by the interplay of two mechanisms: photoionization heating by the ultraviolet background (UVB) radiation and adiabatic cooling due to the expansion of the universe. Assuming a power-law relationship for the temperature-density relation we can express the

equation of state as

$$T(\Delta) = T_0 \Delta^{\gamma-1}, \quad (1)$$

where $\Delta = \rho/\bar{\rho}$, ρ is the matter density field, and $\bar{\rho}$ denotes the mean density of the universe. The temperature at mean density is denoted by T_0 and the parameter $\gamma - 1$ describes the slope of this temperature-density relation indicating whether overdense regions in the universe are hotter than underdense voids (i.e. $\gamma > 1.0$) or vice versa (i.e. inverted temperature-density relation, $\gamma < 1.0$).

Statistical properties of the transmitted flux in the Ly α forest, such as the probability distribution function (PDF) or the line-of-sight power spectrum, provide information about the underlying physics governing the IGM and hence the thermal evolution of the universe (see e.g. McDonald et al. 2000; Weinberg et al. 2003; Meiksin 2009). The Ly α flux PDF — although dependent on all thermal parameters — is particularly sensitive to the value of the slope parameter γ of the temperature-density relation, that provides valuable insights into the thermal state of the IGM, and thus the PDF represents a useful tool to obtain constraints on it (Jenkins & Ostriker 1991). Several studies using this statistical approach to infer γ have found evidence for an inverted, i.e. $\gamma < 1.0$ (see e.g. Becker et al. 2007; Viel et al. 2009; Bolton et al. 2008; Rorai et al. 2016) or isothermal, i.e. $\gamma \approx 1.0$ (see e.g. Calura et al. 2012; Garzilli et al. 2012), temperature-density relation of the IGM. However, an inverted temperature-density relation contrasts with the theoretically predicted value of $\gamma \approx 1.6$ for a post-reionization IGM (see e.g. Hui & Gnedin 1997; Hui & Haiman 2003; McQuinn & Upton Sanderbeck 2015). Furthermore, it has proven to be difficult to explain an in-

* email: eilers@mpia.de

¹ Max-Planck-Institute for Astronomy, Königstuhl 17, 69117 Heidelberg, Germany; eilers@mpia.de

² International Max Planck Research School for Astronomy & Cosmic Physics at the University of Heidelberg

³ Physics Department, University of California, Santa Barbara, CA 93106-9530, USA

⁴ Lawrence Berkeley National Laboratory, Berkeley, CA 94720, USA

verted temperature-density relation. Blazar heating has been suggested as a possible mechanism to cause an inverted relation (e.g. Puchwein et al. 2012; Broderick et al. 2012; Chang et al. 2012; Pfrommer et al. 2012), as well as additional heating of the IGM due to He II reionization (e.g. Bolton et al. 2008; Furlanetto & Oh 2008; McQuinn et al. 2009; Meiksin & Tittley 2012; Compostella et al. 2013). However, both mechanisms fail to reproduce an inverted temperature-density relation at typical densities around $z \approx 3$.

Other attempts to constrain γ from the Ly α flux PDF, did not find evidence for an inverted temperature-density relation (see e.g. Rollinde et al. 2013; Lee et al. 2015). The one-dimensional power spectrum has also been applied to obtain constraints on γ (e.g. McDonald et al. 2000; Zaldarriaga et al. 2001, 2003). These studies favor a slope parameter of $\gamma > 1.0$, which is more consistent with the canonical value of $\gamma \approx 1.6$. Other techniques to infer γ such as wavelet decomposition (e.g. Theuns & Zaroubi 2000; Lidz et al. 2010) or the measurement of Doppler parameters and column densities of individual Ly α forest absorbers (e.g. Rudie et al. 2012; Bolton et al. 2014; McDonald et al. 2001; Schaye et al. 2000) lead to similar estimates of $\gamma \approx 1.3 - 1.6$.

The reason for the differences between the estimates of the slope parameter γ of the temperature-density relation are still debated in the literature, since the various techniques have different sources of systematic uncertainties. In this paper we will focus on the Ly α flux PDF, which seems to be giving the widest spread of values for the estimate of γ . One challenge and the biggest source of uncertainty when working with the PDF is that it requires precise estimates of the quasar continuum level for each quasar spectrum, since imprecise continuum fitting can result in biases (see e.g. Desjacques et al. 2007; Lee 2012). Kim et al. (2007) show that different continuum fitting strategies applied to the same data set can result in significant differences in the resulting PDF and hence varying estimates for γ . Faucher-Giguère et al. (2008) show that the magnitude of the bias in the continuum estimation increases with redshift, since it becomes more and more difficult to estimate the unabsorbed continuum level for quasars at $z \gtrsim 4$ due to increased Ly α absorption. Lee (2012) also pointed out that the quasar continuum fit is dependent on the underlying model of the IGM. Thus depending on the true underlying value of γ one is more likely to over- or underestimate the quasar continua. A larger (smaller) value of γ leads to an under (over) -estimation of the continuum level. In order to avoid likely biases due to continuum fitting by hand, Lee et al. (2012) introduced mean-flux-regulated principal component analysis (PCA) continuum fitting, where PCA fitting is carried out on wavelengths longer than the Ly α emission line in order to provide a prediction for the shape of the Ly α forest continuum. The slope and amplitude of this continuum prediction is then corrected using external constraints for the Ly α forest mean flux.

A similar approach for handling continuum uncertainties in the estimation of the flux PDF has been presented by Rorai et al. (2016) recently, who reduced the sensitivity of the PDF to these uncertainties by calculating the flux PDF from a ‘regulated’ flux level, defined as the transmitted flux divided by the 95th percentile of the flux distribution within a spectral region of 10 Mpc h^{-1} .

The advantage of regulating the transmitted flux by the 95th percentile of the flux distribution compared to the mean flux is, that the 95th percentile of the flux falls near the peak of the flux PDF for all IGM models and is therefore less noisy than the mean flux, which falls in a flux interval with low probability.

In this paper we present a new Bayesian algorithm making use of a Markov Chain Monte Carlo (MCMC) sampling that allows us to simultaneously estimate the unknown continuum of each quasar in an ensemble of high-resolution spectra as well as their common Ly α forest flux PDF. This fully automated PDF regulated continuum fitting method models the unknown quasar continuum with a PCA with the coefficients of the principal components treated as nuisance parameters. This method allows us to estimate parameters governing the thermal state of the IGM, such as the slope parameter of the temperature-density relation γ , while marginalizing out continuum uncertainties in a fully Bayesian way. We are thus also able to investigate any degeneracies between the uncertainties in the continuum estimation and the thermal properties of the IGM.

The paper is structured as follows. In § 2 we describe our method for generating mock data of high-resolution quasar spectra with a lognormal model for Ly α forest absorption required to develop our analysis algorithm. In § 3 we introduce the likelihood function of the PDF of the transmitted Ly α forest flux and explain how it can be used to simultaneously estimate the quasar continuum level and the thermal properties of the IGM governing the shape of the PDF. In § 4 we present the results of our analysis at two different redshifts, $z = 3$ and $z = 5$, and study the degeneracies between thermal parameters of the IGM and continuum uncertainties. We discuss and summarize our key results in § 5 and § 6.

2. MOCK QUASAR SPECTRA WITH LY α FOREST ABSORPTION

In this section we describe a method to generate matter density fields in order to create mock Ly α forest absorption spectra. This Ly α forest model can then be used to generate realistic mock quasar spectra by multiplying the absorption field with a quasar continuum level.

2.1. A Semi-Analytic Model for Ly α Forest Absorption

The fluctuating Gunn-Peterson approximation (FGPA, see e.g. Weinberg et al. 1998; Croft et al. 1998, 1999) provides a relationship between the observed flux in the Ly α forest and the underlying matter density distribution. It represents a valuable tool for generating Ly α absorption spectra from cosmic matter density fields, which we will use to generate mock quasar spectra. Assuming that the intergalactic gas is in photoionization equilibrium and follows the temperature-density relation in eqn. (1), the optical depth τ of the IGM scales with the matter density contrast as

$$\tau \propto \Delta^{2-0.7(\gamma-1)}. \quad (2)$$

The normalized transmitted flux F in the Ly α forest is related to the intervening optical depth of the photoionized gas by

$$F = \exp(-\tau). \quad (3)$$

Combining eqn. (2) and eqn. (3) leads to a relationship between the transmitted flux F and the matter density contrast Δ .

McDonald et al. (2006) provide a semi-analytic model to generate absorption fields for the Ly α forest from matter density fields based on the lognormal model introduced by Bi et al. (1992) and Bi & Davidsen (1997). The goal of this semi-analytic model is to generate realistic flux fields F that approximately reproduce both the observed power spectrum as a function of wave number k and redshift z and the observed PDF of the Ly α forest. We introduce small modifications to this model in order to accommodate different values for γ in the temperature-density relation, and summarize its main features below.

The generation of each F field for the i th quasar spectrum begins by creating an initial Gaussian random field $\delta_{i,0}$ representing the underlying dark matter density contrast with a power spectrum given by:

$$P_\delta(k) = \frac{1 + \left(\frac{0.01\text{s/km}^{-1}}{k_0}\right)^\nu}{1 + \left(\frac{k}{k_0}\right)^\nu} \exp\left[-(kR_\delta)^2\right], \quad (4)$$

with values of $k_0 = 0.001$ s/km, $\nu = 0.7$, $R_\delta = 5.0$ km/s, that were chosen to approximately reproduce the dependence on wave number k in the observed flux power spectrum of the Ly α forest. An evolution of the amplitude $A(z)$ of the density fluctuations with redshift is introduced by the transformation

$$\delta_i = A(z_i)\delta_{i,0} \quad (5)$$

with

$$A^2(z_i) = 58.6 \left(\frac{1+z_i}{4}\right)^{-2.82}. \quad (6)$$

The values for the amplitude and exponent here were chosen such that the final flux power spectrum would evolve like the observed one. In order to obtain the density field n_i of the baryonic diffuse matter of the IGM we do not use the squared lognormal transformation that has been used in previous work (see e.g. Bi et al. 1992; Bi & Davidsen 1997; McDonald et al. 2006), but instead use a lognormal transformation with an exponent of $2-\beta$ with $\beta = 0.7(\gamma-1)$. This step introduces the dependence on the slope parameter γ of the temperature-density relation of the IGM that we are interested in. Hence the transformation of the density field n_i is computed as

$$n_i = n_0 \left[\exp\left(\delta_i - \left\langle \frac{\sigma_i^2}{2} \right\rangle\right) \right]^{2-0.7(\gamma-1)}, \quad (7)$$

where n_0 is the mean number density of the IGM. The factor σ_i^2 is computed from the input density power spectrum in eqn. (4) and fixes the mean of the lognormal field to unity.

After the transformation the n_i field is smoothed with a Gaussian filter with standard deviation $\sigma_\tau = 20$ km s $^{-1}$. Note that the quasar spectra that we will consider in this work have a resolution comparable to the achievable resolution of echelle spectrographs (see § 2.3 for details), which is higher than the here applied Gaussian filter. However, since this smoothing is applied to the n_i

field and not to the flux F itself, it accounts for the effects that give rise to the velocity width of the Ly α forest lines, such as thermal broadening, Jeans pressure smoothing (see Gnedin & Hui 1998; Rorai et al. 2013; Kulkarni et al. 2015; Oñorbe et al. 2016), or peculiar velocities and velocities due to the Hubble flow. We then multiply with a redshift evolution factor of $0.374[(1+z_i)/4]^{5.1}$ (the form of this factor is again chosen to reproduce the observations) to produce a field τ . The transmitted flux can then be calculated with eqn. (3).

Note that this simple toy model of the IGM only accommodates a dependency on the thermal parameter γ and ignores dependencies on the temperature T_0 or the pressure smoothing scale λ_P . However, Bolton et al. (2008) used hydrodynamical simulations to show that the Ly α flux PDF is mostly sensitive to γ , whereas the other thermal parameters introduce only relatively modest changes to its shape. If we would apply our method to real quasar spectra the simple model adopted here would clearly be insufficient, but rather we would use hydrodynamical simulations that accommodate dependencies on all thermal parameters. However, the main advantage of this model is that it is fast and a large grid of models can be generated quickly. We will comment more on this later and argue that future augmentation of the parameter space of the PDF should be easy to incorporate.

We re-scale the optical depth in order to obtain values for the mean flux of our mock Ly α forest spectra that are consistent with the measurements of Faucher-Giguère et al. (2008) at redshift $z = 3$, i.e. $\langle F \rangle \approx 0.680$. For an estimate of the mean flux at $z = 5$ we use the fitting formula presented in Oñorbe et al. (2016), because the measurements of the mean flux do not extend past $z > 4.85$, and obtain $\langle F \rangle \approx 0.189$ at redshift $z = 5$.

Fig. 1 illustrates the effect of changing the slope parameter γ on the flux PDF at redshifts of $z = 3$ and $z = 5$ in the left and right panel, respectively. Decreasing γ increases the temperature in the underdense regions of the IGM, i.e. $\Delta < 1.0$, according to the temperature-density relation (see eqn. (1)). Higher temperatures cause the hydrogen recombination rate to decrease, therefore reducing the fraction of neutral H I and the Ly α optical depth, which in turn increases the transmitted flux in these regions. These differences are apparent at $F > 0.5$, where the peak of the flux PDF shifts towards higher values for lower values of γ . Accordingly, by measuring the Ly α flux PDF one can constrain the parameter γ .

2.2. Empirical Quasar Continua

In order to generate mock quasar spectra we multiply Ly α absorption fields with quasar continua. For this purpose we use the estimated continua of 50 real quasar spectra taken by the Hubble Space Telescope (HST) Faint Object Spectrograph (FOS) from Suzuki et al. (2005), which were collected and calibrated by Bechtold et al. (2002). All quasars in this sample have complete wavelength coverage from 1020 Å to 1600 Å in the rest frame. These moderate resolution spectra ($R \sim 1300$) have been combined from several exposures, brought into the rest frame and re-binned into pixels of size 0.5 Å. The average signal-to-noise ratio of the chosen quasar sample is $\langle S/N \rangle = 19.5$ per 0.5 Å pixel, and quasars with $S/N < 10$ per pixel were removed from the sample.

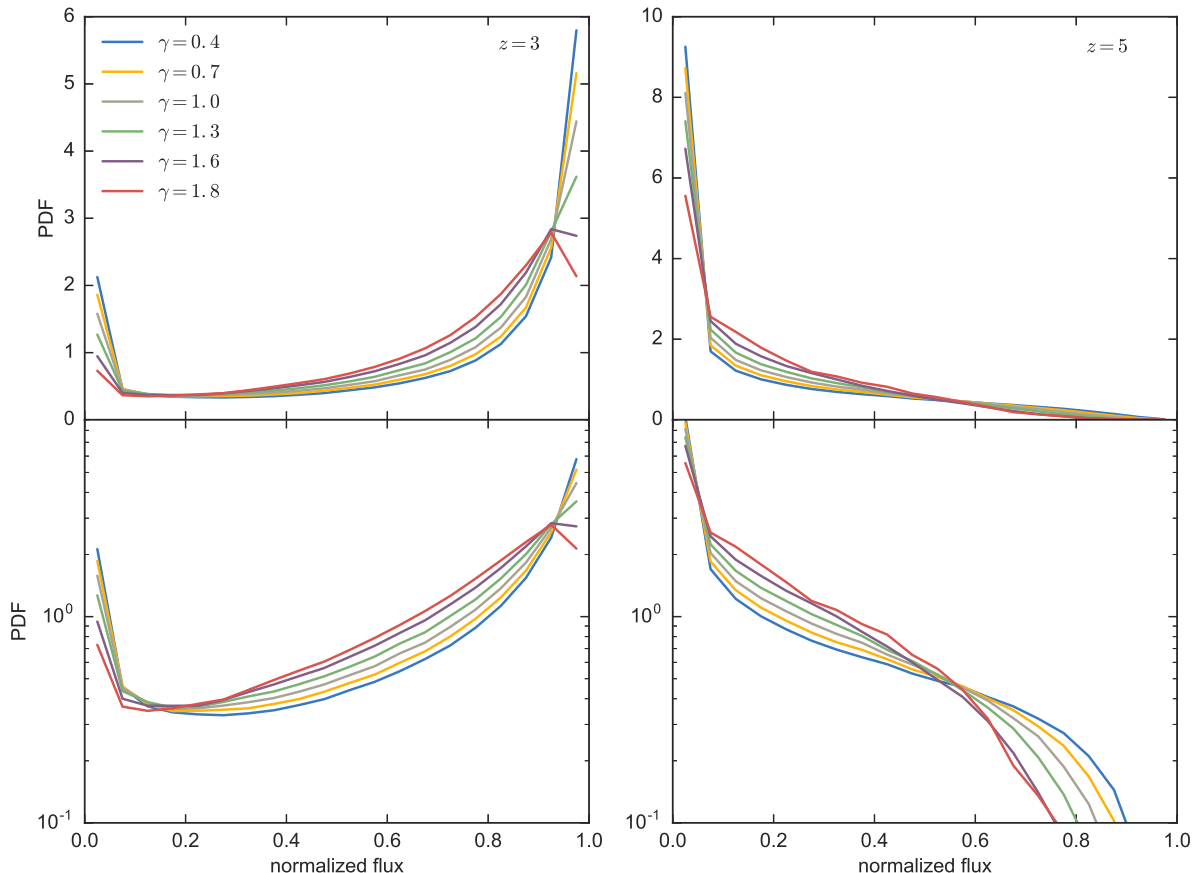


FIG. 1.— The PDF of the transmitted flux in the Ly α forest in bins of $\Delta F = 0.05$ from noise-free mock quasar spectra at two different redshifts, $z = 3$ (left panels) and $z = 5$ (right panels). The different colored PDF's account for different values of the slope parameter γ of the temperature-density relation of the IGM.

All quasar spectra have been renormalized to unity at 1280 Å in the rest-frame. The quasars in the sample are at very low redshifts in the range $0.14 < z < 1.04$ with a mean redshift of $\langle z \rangle = 0.58$. Quasars at these low redshifts show very few Ly α absorption lines, which makes it easier to correctly estimate their continuum level. Spectra with broad absorption lines or damped Ly α systems were excluded from the sample, because of the associated large uncertainties in placing their continuum level. In order to obtain precise and smooth continuum estimations for these spectra, Suzuki et al. (2005) fitted Chebyshev polynomials of different orders to each HST spectrum and applied further fine-tuning adjustments afterwards using a B -spline fit. For more details on this procedure we refer the reader to Suzuki et al. (2005). We use these smoothed continua as the *true* continua of our mock quasar spectra.

2.3. Mock Quasar Spectra

We multiply the empirical quasar continua with different realizations of the Ly α forest absorption field to produce mock quasar spectra. To simplify the analysis we assume no redshift evolution of the quasar continua. The absorption fields are also generated at a fixed redshift, and there is thus no redshift evolution in the Ly α forest along the quasar sightline. These assumptions should

not alter the conclusions of this work. Thus we generate our own mock spectra by multiplying the Ly α forest F at different redshifts into the quasar continua in the wavelength region where Ly α forest is usually found, i.e. between Ly β (1025.18 Å) and Ly α (1215.67 Å) emission.

We choose the pixel size and resolution of our mock spectra to be comparable to real high resolution spectra taken with the Ultraviolet and Visual Echelle Spectrograph (UVES) at the Very Large Telescope (VLT) and the High Resolution Echelle Spectrometer (HIRES) from the Keck telescope. Since the pixel size from these spectrographs is smaller than the pixel size of 0.5 Å used by Suzuki et al. (2005), we interpolate the HST continua onto a finer grid with the desired pixel scale, which we chose to be 2.5 km/s. We then add random white noise to our mock data, i.e. we ignore correlations between the noise and the transmission, with a signal-to-noise ratio that is achievable with UVES or HIRES. The highest quality quasar spectra at $z \sim 3$ from these instruments achieve a signal-to-noise ratio in the Ly α forest of $S/N \approx 80$ per 6 km/s resolution element (see e.g. Dall'Aglio et al. 2008; Lehner et al. 2014; O'Meara et al. 2015). For our purposes we assume a slightly larger resolution element of 10 km/s, which gives a signal-to-noise ratio of $S/N \approx 103$ per resolution element, assuming the same noise properties. A pixel size of 2.5 km/s implies 4 pixels per resolution element, and thus we obtain a signal

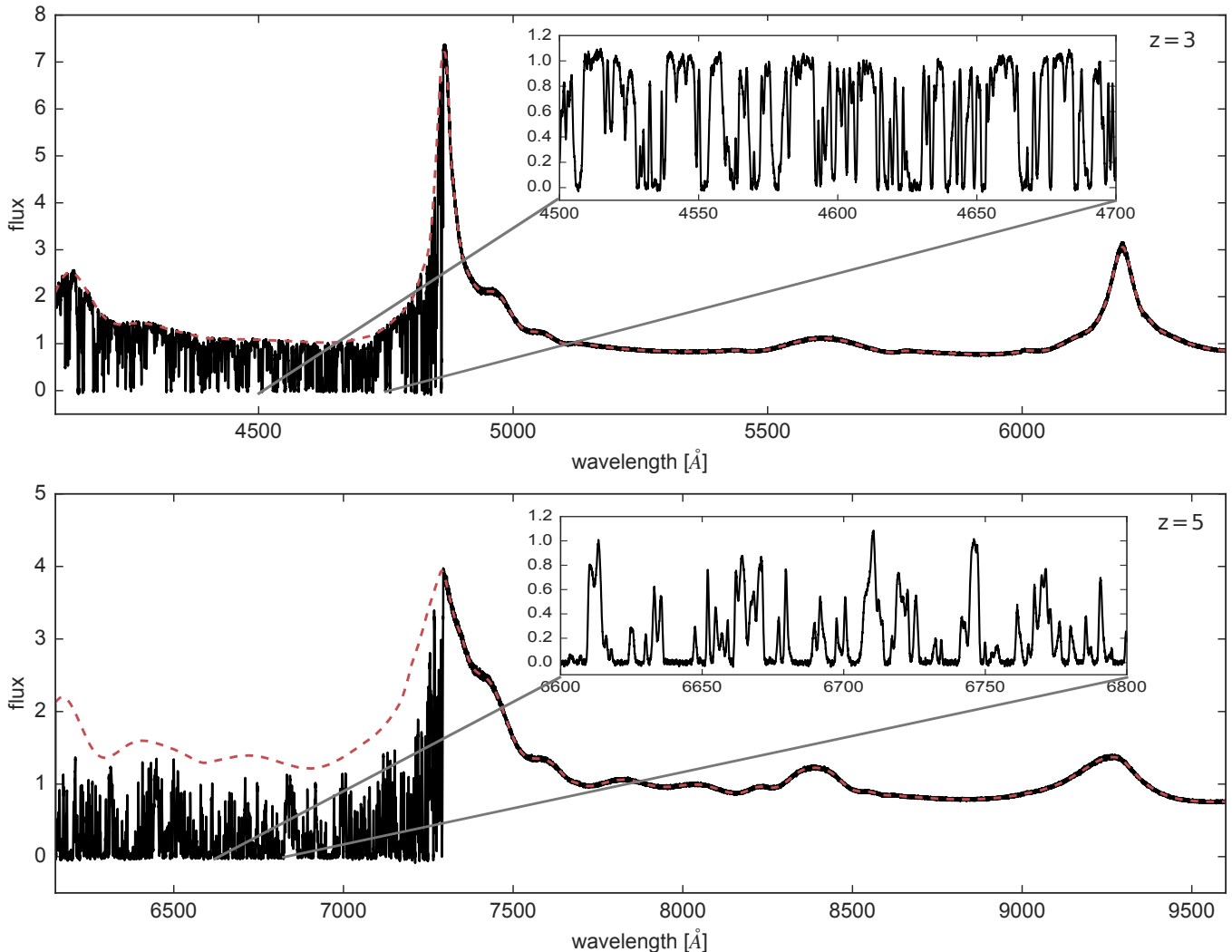


FIG. 2.— Examples of the generated mock quasar spectra at two different redshifts, $z = 3$ (upper panel) and $z = 5$ (lower panel). The red dashed lines indicate the quasar continuum from one of the HST spectra from Suzuki et al. (2005). The black curves show the resulting quasar spectra with $\text{Ly}\alpha$ forest absorption added between the $\text{Ly}\alpha$ and $\text{Ly}\beta$ emission. The insets show a zoom into the respective $\text{Ly}\alpha$ forests, after normalizing by the quasar continuum. The mock $\text{Ly}\alpha$ forest was created assuming a value of $\gamma = 1.0$.

to noise ratio of $S/N \approx 51$ per pixel. For quasars at $z \sim 5$ we will assume a lower signal-to-noise ratio of $S/N \approx 20$ per pixel, consistent with existing high resolution quasar spectra at this redshift (Calverley et al. 2011). However, we will see in § 3.2 that our results at $z = 5$ are fairly independent of the exact noise level, because the $\text{Ly}\alpha$ flux PDF at these redshifts is only mildly sensitive to noise. We add Gaussian distributed white noise to our mock quasar spectra with a standard deviation $\sigma_{\text{noise}} = \frac{\langle F \rangle}{S/N}$, where $\langle F \rangle$ is the mean transmitted flux and $S/N \approx 51$ or $S/N \approx 20$ for spectra at $z \sim 3$ and $z \sim 5$, respectively. Examples of our mock quasar spectra at redshift $z = 3$ and $z = 5$ are presented in Fig. 2.

3. QUASAR CONTINUUM ESTIMATION VIA PDF REGULATION

In this section we first describe the PCA basis that we will use to model the continuum of each quasar. We then examine the impact of uncertainties in the continuum estimation and spectral noise on the flux PDF. Then we demonstrate the necessity of incorporating these contin-

uum uncertainties and noise into models of the PDF in order to avoid introducing biased estimates of thermal parameters. Finally, we introduce the likelihood function \mathcal{L}_{PDF} that is the basis of our Bayesian algorithm, and show how it enables us to simultaneously estimate the parameters governing the flux PDF and quasar continua.

3.1. Modeling the Quasar Continuum with Principal Component Analysis

The quasar continuum is modeled using a PCA enabling us to describe the continuum shape via a simple linear model. Suzuki (2006) analyzed the shape of 50 HST quasar spectra and established a set of principal component spectra (PCS) that reproduce the continuum shape of each quasar with high accuracy. This accuracy in the continuum model is crucial, in order to prevent biases when studying the statistical properties of the $\text{Ly}\alpha$ forest.

The idea of the PCA is to represent the continuum spectrum $|q_{i,\lambda}\rangle$ of the i th quasar by a reconstructed spec-

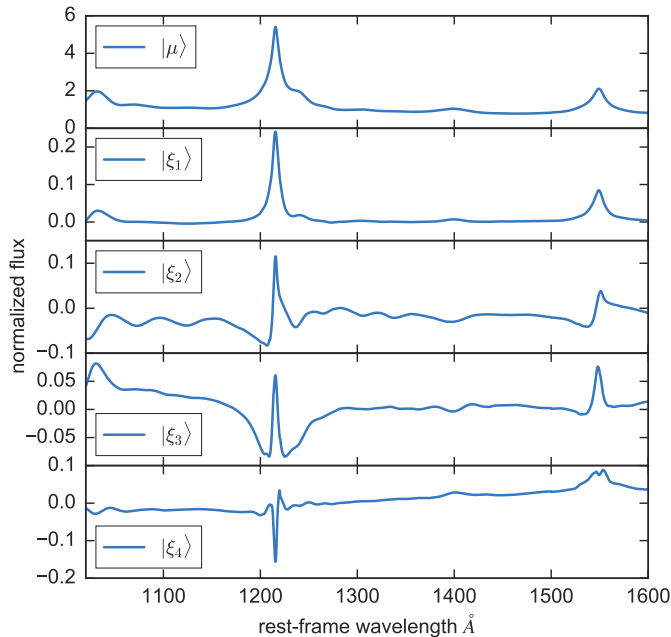


FIG. 3.— Mean quasar spectrum $|\mu\rangle$ and the first four PCS $|\xi_i\rangle$ from Suzuki (2006).

trum that consists of a mean spectrum $|\mu_\lambda\rangle$ and a sum of m weighted PCS $|\xi_{j,\lambda}\rangle$, where the index λ denotes the wavelength. Hence

$$|q_{i,\lambda}\rangle \approx |\mu_\lambda\rangle + \sum_{j=1}^m \alpha_{ij} |\xi_{j,\lambda}\rangle, \quad (8)$$

where $|\xi_{j,\lambda}\rangle$ refers to the j th PCS and α_{ij} is its weight for quasar i .

Suzuki (2006) derived ten PCS, which are shown in Fig. 2 and Fig. 3 of their paper. We show their mean quasar spectrum and the first four PCS in Fig. 3. The more components are included in the reconstruction, the lower the variance of the individual spectra about the model fits. Table 1 in Suzuki (2006) summarizes the fraction of the variance accounted for depending on the number of principal components employed.

In our analysis we will vary the number of PCS that we include when estimating the quasar continuum. Since we are only taking a finite number of components we cannot account for the total variance seen in quasar spectra and thus we inevitably introduce an error in the continuum fit. In order to analyze the best precision possible for a chosen PCA basis, we estimate the continuum model coefficients by using a Markov Chain Monte Carlo (MCMC) algorithm to sample the likelihood function $\mathcal{L} = \exp(-\chi^2/2)$ with

$$\chi^2 = \sum_{\lambda} \frac{(C_{\text{data},i\lambda} - C_{\text{model},i\lambda}(\alpha_{ij}))^2}{\sigma_{i,\text{noise}}^2}. \quad (9)$$

Here $C_{\text{data},i\lambda}$ is the true quasar continuum determined by Suzuki et al. (2005) (see § 2.2), $C_{\text{model},i\lambda}$ is the model continuum from eqn. (8), and $\sigma_{i,\text{noise}}$ is the standard deviation of the white noise added to each spectrum. We use the means of the posterior probability distributions of each coefficient α_{ij} as our best continuum model for

quasar i . Note that for this estimation we take all pixels in the whole available wavelength range, i.e. between 1020 Å and 1600 Å, into account and that we do not add artificial Ly α forest to the true quasar continua here. We then evaluate the precision of the estimated continuum model by calculating the continuum residuals, i.e. the relative continuum error,

$$\Delta C/C = \frac{C_{\text{data},\lambda} - C_{\text{model},\lambda}}{C_{\text{data},\lambda}}, \quad (10)$$

only in the wavelength range that we are particularly interested in, i.e. the Ly α forest region between the Ly β and Ly α emission peak. However, in order to avoid biases due to the influence of proximity zones, and to guarantee that we exclude the Ly β forest in the presence of quasar redshift errors, we only include the wavelengths between 1040 Å to 1190 Å. Note that all our mock spectra use the true quasar continua determined from the HST spectra.

The relative continuum error $\Delta C/C$ is shown in the upper panel of Fig. 4 for different numbers of PCS. The distribution for the ensemble of *all* 50 spectra follows a Gaussian distribution reasonably well. Note that this is not necessarily the case for a fit to a single quasar spectrum. The Gaussian distribution has a standard deviation of $\sigma_{\text{PCA}} \approx 3.0\%$ when all ten components are used to reconstruct the continuum spectra (blue histogram). Fewer components, i.e. $N_{\text{PCA}} = 2$ (gray histogram) or $N_{\text{PCA}} = 4$ (yellow histogram), account for less individual variance in the spectra and thus decrease the precision of the estimated continuum and hence increase the width of the distribution of continuum residuals. The middle and lower panels of Fig. 4 plot the mean μ_{PCA} and standard deviation σ_{PCA} of the relative continuum error as a function of N_{PCA} used to reconstruct the continuum. Increasing the number of PCS implies a more precise, i.e. decreasing σ_{PCA} , and less biased, i.e. decreasing $|\mu_{\text{PCA}}|$, estimation of the quasar continua in the Ly α forest region.

3.2. Models of the PDF of the Transmitted Ly α Forest Flux

In order to calculate the PDF of the transmitted flux in the Ly α forest, the flux in the quasar spectra has to be normalized by its continuum level. However, the exact placement of the continuum level is very challenging, because, particularly at higher redshifts, much of the continuum flux is absorbed by the Ly α forest. Thus one should consider the finite precision with which the continuum can be estimated. If one instead adopts a PCA model, as is done here, this continuum model has limited precision due to the finite number of PCS, and thus additionally has an intrinsic uncertainty which we quantified in the previous subsection (see Fig. 4).

We will now analyze the effects of a misplaced or imprecise continuum level and the effects of noise in the spectra on the shape of the PDF. In the presence of noise and continuum errors the continuum normalized transmitted flux, which we denote as f , can take on values below 0 and above 1. We describe the level of uncertainty in the continuum normalized flux caused by the continuum error with σ_C . Note that we expect σ_C to take on values comparable to or slightly larger than the intrinsic PCA continuum model error σ_{PCA} (see Fig. 4), since σ_{PCA}

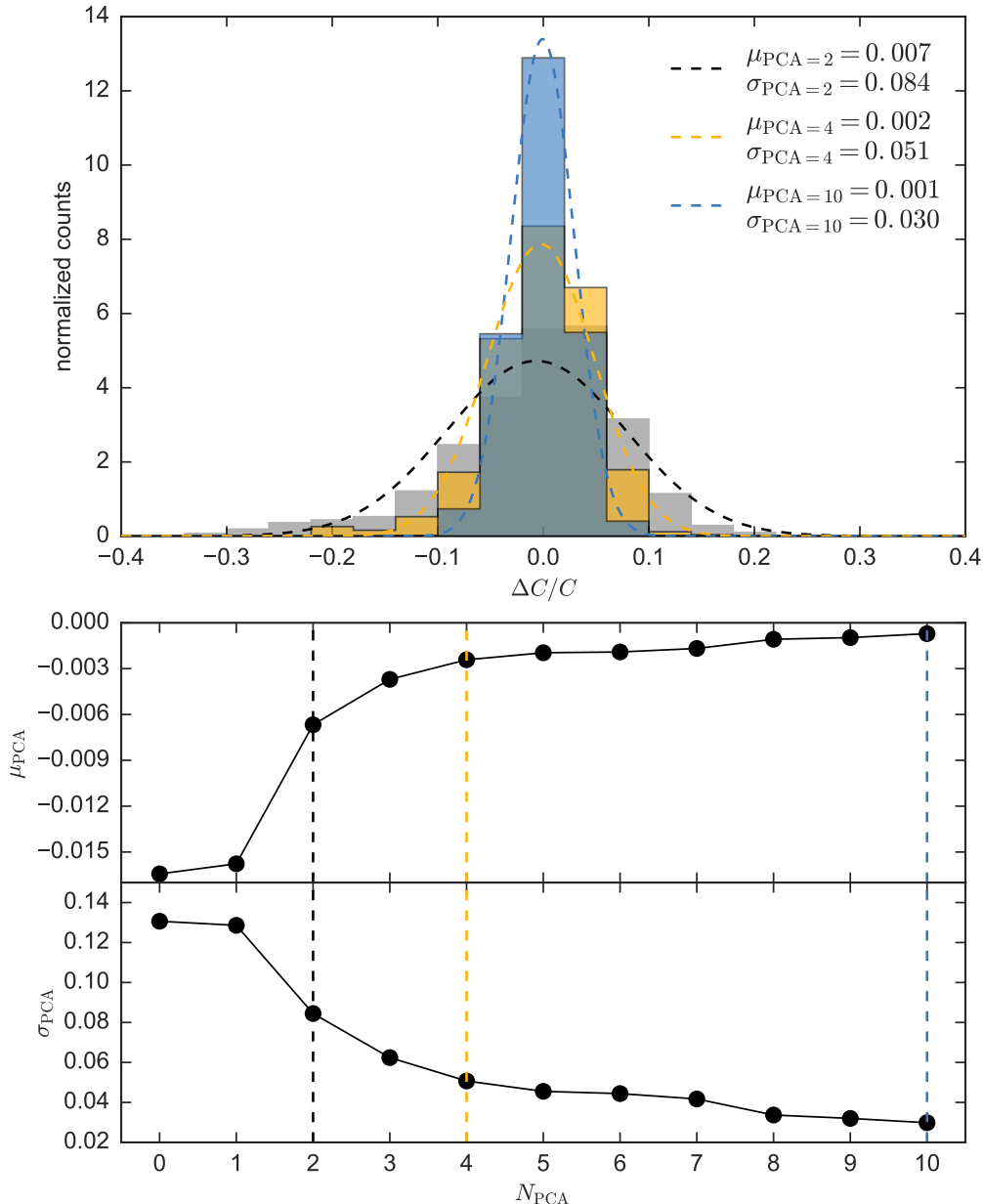


FIG. 4.— *Upper panel:* Distribution of continuum residuals, i.e. relative continuum errors, $\Delta C/C$ in the continuum estimation of 50 HST spectra when the quasar continua are fitted to the whole available spectral range. The blue histogram shows the relative continuum errors when ten PCS were taken into account in the continuum model, whereas the yellow histogram shows the same for four components and the black histogram for two components. The dotted lines show the corresponding Gaussian distributions with the same mean and standard deviation. *Middle Panel:* The mean of the continuum residual distribution versus the number of PCS, N_{PCA} , in the continuum model. The dashed vertical lines correspond to the relative continuum errors shown in the upper panel. *Bottom panel:* The standard deviation of the relative continuum errors versus the number of PCS in the continuum model.

represents the best continuum error one can achieve using the given PCA basis as the continuum model, but the continuum error σ_C could generally be larger. We can approximate the transmitted flux f by modifying the perfectly normalized and noiseless flux F by adding white noise with a standard deviation σ_{noise} and introducing the effects of the continuum errors in the following way:

$$f = \frac{F + \mathcal{N}(0, 1)\sigma_{\text{noise}}}{1 + \mathcal{N}(0, 1)\sigma_C}, \quad (11)$$

where $\mathcal{N}(0, 1)$ represents a random draw from a normal

Gaussian distribution with mean $\mu = 0$ and standard deviation $\sigma = 1$. Note that the numerator in eqn. (11) adds random white noise to the perfectly normalized transmitted flux, whereas the denominator introduces the effects of continuum errors.

In Fig. 4 we have seen that the relative continuum errors $\Delta C/C$ of the ensemble of all 50 quasars follows a Gaussian distribution. Hence, we can generate PDF models that incorporate the uncertainty in the continuum model by simply drawing Gaussian deviates with a standard deviation of the continuum error σ_C and adding them to each flux pixel in the Ly α forest to mock up

the continuum error. In this way we generate a new set of models for the transmitted Ly α forest flux PDF that incorporate the continuum errors as well as the effects of spectral noise. This new set of PDF models now has *two* free parameters: the slope parameter γ of the temperature-density relation of the IGM, where we consider values of $0.0 \leq \gamma \leq 2.0$ in steps of $\Delta\gamma = 0.01$ for our PDF models, and additionally, the continuum error σ_C that we allow to vary between 0.5% and 15.0% in steps of $\Delta\sigma_C = 0.1\%$. The grid of PDF models is generated by averaging over many realizations of approximately normalized mock Ly α forests for every combination of the two free parameters γ and σ_C .

In Fig. 5 we demonstrate the effects of continuum error and noise on the flux PDF at redshifts $z = 3$ (left panels) and $z = 5$ (right panels), for a fixed value of $\gamma = 1.0$. The different colored curves represent PDF models constructed from mock Ly α forest spectra with different levels of continuum error added. The black curve shows the PDF taken from perfect mock Ly α forests without any continuum error or noise. There is an obvious difference between the PDF's at redshift $z = 3$ and those at $z = 5$. Whereas at redshift $z = 3$, one can clearly distinguish the different PDF models depending on the underlying continuum error, these differences are hardly noticeable at redshift $z = 5$. The continuum errors have only a weak impact on the shape of the PDF at the higher redshift, which can be understood as follows.

The PDF is a function of the approximately normalized Ly α forest flux f , which itself is a function of the continuum error as shown in eqn. (11). Thus:

$$\Delta\text{PDF} = \frac{d\text{PDF}}{df} \frac{df}{d\sigma_C} \Delta\sigma_C \quad (12)$$

The first term $\frac{d\text{PDF}}{df} \approx \frac{d\text{PDF}}{dF}$ indicates that the change in the PDF is dependent on the slope of the PDF itself, thus the steeper the PDF is, the larger the change with varying σ_C . This can be clearly seen in the PDF at $z = 3$ (left panel of Fig. 5): at fluxes around $0.8 \lesssim f \lesssim 1.0$ the PDF has a steep slope such that the term $\frac{d\text{PDF}}{df}$ is large, as are the differences in the PDF models for the different values of σ_C . Whereas at smaller flux values of $0.2 \lesssim f \lesssim 0.8$ the slope of the PDF $\frac{d\text{PDF}}{df}$ is smaller, as are the differences in the PDF models. But that explanation is not sufficient, because the PDF is also steep for very small flux values around $f \approx 0.1$ at $z = 3$ as well as at $z = 5$. At these small fluxes there is no change in the PDF models visible for different values of σ_C because of the second term of eqn. (12) $\frac{df}{d\sigma_C} = \left| \frac{f}{1+N(0,1)\sigma_C} \right|$ that indicates the change in the PDF is also dependent on the actual flux level f . Hence for small fluxes $f \approx 0.1$ there is a much smaller change in the PDF than at larger flux values $f \approx 1.0$. Thus at $z = 5$ where the flux values are lower overall (the mean flux is $\langle F \rangle = 0.189$), there is very little change in the PDF when the continuum error σ_C is increased. This implies that at lower redshifts the PDF is very sensitive to continuum errors, whereas at higher redshift the sensitivity is much lower, which is illustrated in Fig. 5.

3.3. The Likelihood Function

In order to estimate model parameters from measurements of the flux PDF, we introduce a likelihood function \mathcal{L}_{PDF} . The PDF models are explicitly dependent on two free parameters, the physical parameter γ and the continuum error σ_C . In addition there is an implicit dependence on the parameters of the quasar continuum model, i.e. the coefficients α_{ij} of the PCS for each quasar (see eqn. (8)), since each spectrum needs to be divided by its estimated continuum level in order to normalize the transmitted Ly α forest flux before calculating the flux PDF. Thus the likelihood function has a multi-variate Gaussian form and is given by the following equation:

$$\begin{aligned} \mathcal{L}_{\text{PDF}} &= \mathcal{L}(\gamma, \sigma_C, \alpha_{ij} | \text{PDF}_{\text{data}}) \\ &= \frac{1}{\sqrt{\det(\mathbf{C})}} \exp\left(-\frac{1}{2} \mathbf{d}^T \mathbf{C}^{-1} \mathbf{d}\right). \end{aligned} \quad (13)$$

Here \mathbf{C} represents the covariance matrix governing the covariances between the different flux bins in the PDF. The vector \mathbf{d} denotes, the difference between the calculated flux PDF and the model PDF for each bin:

$$\mathbf{d} = \text{PDF}_{\text{data}} - \text{PDF}_{\text{model}}(\gamma, \sigma_C, \alpha_{ij}). \quad (14)$$

Our new Bayesian formalism is based on this likelihood function \mathcal{L}_{PDF} which we sample with a MCMC algorithm. The goal of an MCMC is to draw samples from a complex probability distribution for which direct sampling is challenging, thus providing an approximate representation of the true posterior probability distribution of the model parameters. For our MCMC algorithm we employ the python implementation *emcee*, which is described in detail by Foreman-Mackey et al. (2013). An important advantage of this algorithm compared to other codes is its affine-invariance property, first proposed by Goodman & Weare (2010). This makes the algorithm insensitive to any covariances among the parameters and requires hand-tuning of only one or two parameters compared to $\sim N^2$ for a traditional algorithm in an N -dimensional parameter space. Another useful property of the *emcee* implementation is that the parameter space is explored by a set of chains, so-called walkers, that evolve in parallel as an ensemble, rather than by a single chain. At every step each walker is randomly assigned to a partner walker, moving along lines which connect the single chains to each other. This feature makes the exploration of the parameter space extremely efficient and allows for parallel computing on multi-core processors.

3.4. The Covariance Matrix \mathbf{C}

There are various sources of covariance in the flux PDF. The flux in the Ly α forest contains spatial correlations that give rise to covariances in the flux PDF. The continuum residuals due to continuum estimation errors of the quasar continua will also result in non-diagonal entries in the covariance matrix of the flux PDF. In what follows we will investigate a set of models for the quasar continua that take different numbers of PCS into account, i.e. we vary $N_{\text{PCA}} = 0, 1, 2, 3, 4$. For each of the N_{PCA} that we explore we generate a separate covariance matrix.

To generate the covariance matrix we create a large set of mock quasar spectra as described in § 2. For each mock spectrum, the underlying continuum, which is a

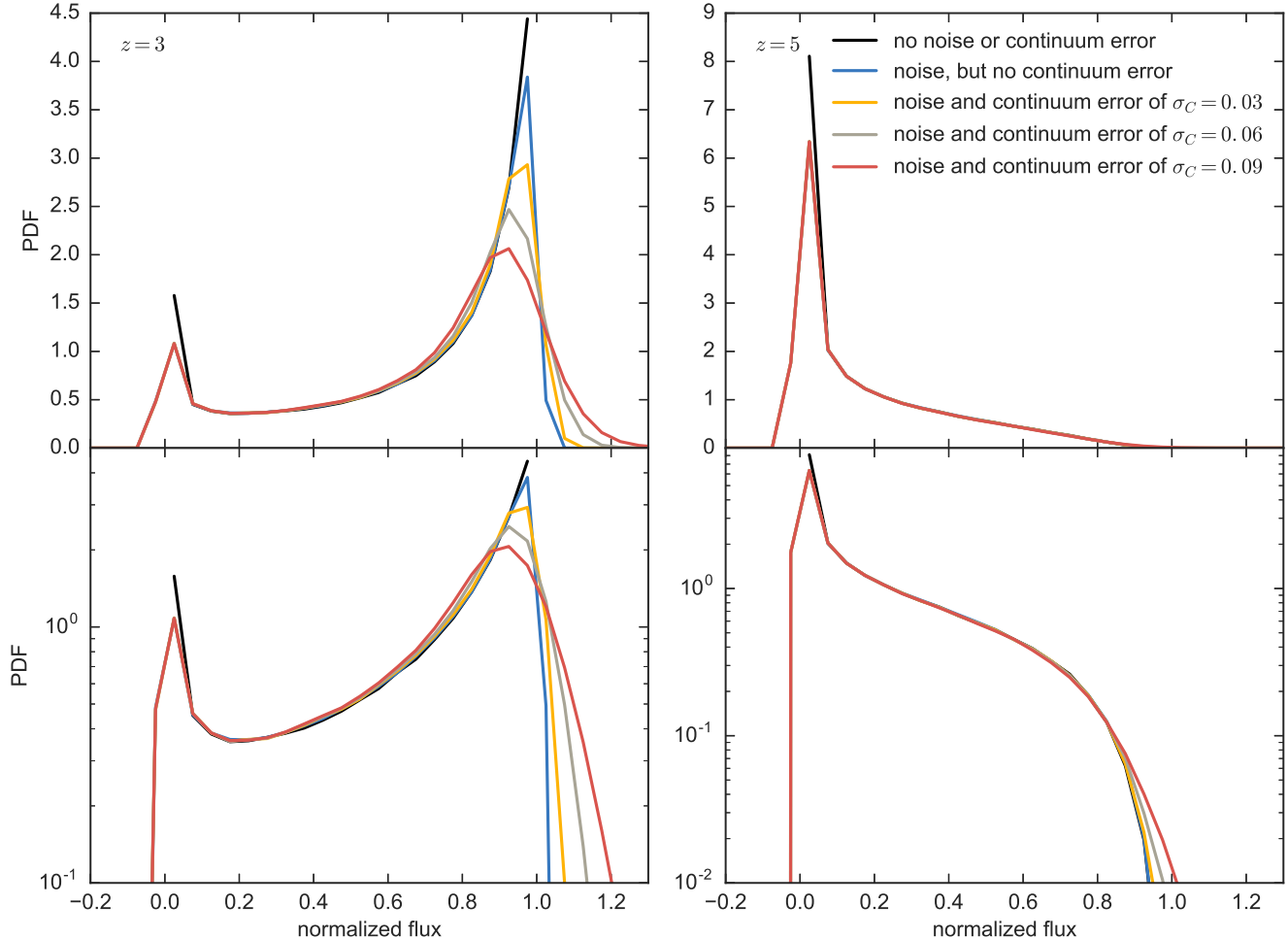


FIG. 5.— PDF's of the flux in the Ly α forest at redshifts of $z = 3$ (left panels) and $z = 5$ (right panels) with different levels of continuum error and noise added to the quasar spectra for a fixed value of $\gamma = 1.0$. The black curves show the unrealistic case of the PDF with noiseless spectra and perfectly known continua. The blue curves show the PDF when random white noise was added to the quasar spectra, but we still assume perfect knowledge of the continuum level. The yellow, gray and red curves show the PDF's with different levels of continuum error, i.e. $\sigma_C = 3\%$, $\sigma_C = 6\%$ and $\sigma_C = 9\%$, and noise added to the spectra, respectively. The plot shows clearly that at a redshift of $z = 3$ the effects of noise and continuum error in the continuum estimation change the shape of the PDF, hence by fitting for the PDF one can obtain constraints on the continuum error. At higher redshifts of $z = 5$ the effects of noise and continuum error do only mildly alter the shape of PDF, since the differences in the blue, yellow, gray and red curves are very small.

draw from the 50 HST spectra, is fit with N_{PCA} PCS in the absence of Ly α forest absorption (see § 3.1). The mock spectrum, which is a product of the true HST continuum times a realization of the Ly α forest, is divided by the approximate PCA continuum model, thus giving approximately normalized Ly α forest spectra with a continuum error that is intrinsic to the continuum model itself. We create many ensembles of N_{QSO} quasar spectra generated in this way, and calculate the PDF of each realization. We use this ensemble of PDF's to calculate the covariances between the different PDF flux bins and obtain a covariance matrix. This covariance matrix now contains the continuum error that is intrinsic to the continuum model with the chosen number of PCS. We chose a fixed value for $\gamma = 1.0$, which we set to be our fiducial value for the mock data set, when generating the covariance matrices.

Note that we consider bins in the PDF in the flux range of $-0.5 \leq f \leq 1.5$. In the absence of contin-

uum error and noise only the bins between $0.0 \leq f \leq 1.0$ would be populated. The inclusion of continuum error and noise will thus populate bins below zero and above one, but for any given γ and N_{PCA} not all flux bins between $-0.5 \leq f \leq 1.5$ will be populated. Indeed the very low and very high end of this range rarely contain any flux pixels, and for a finite number of samples these bins may not be populated such that the resulting covariance matrix is zero. However, models with values of γ significantly different than those used to generate the covariance matrix may actually populate these bins, such that we cannot just neglect the bins and reduce the allowed flux range. The correct approach would clearly be to adopt a more complicated procedure and compute a different covariance matrix for each model, rather than simply fixing γ and N_{PCA} . However, we lack the ability to generate covariance matrices for models with different values of σ_C , other than those intrinsic to the continuum model, i.e. σ_{PCA} , since by construction adding a random

level of continuum error as described in eqn. (11) has no covariance. In this way our covariance matrix is approximate, because we adopt a model with fixed N_{PCA} and an implied single value of $\sigma_C = \sigma_{\text{PCA}}$ to calculate it. This means that the range of values of σ_C we can explore to create covariance matrices is limited and thus results in matrix entries with zero covariance at the edges of the considered flux range.

For simplicity, we opt to proceed with a single covariance matrix (for each employed value of N_{PCA}). In order to prevent the covariance matrix from becoming singular, we apply a technique known as matrix shrinkage and add an identity matrix multiplied with a small value (e.g. Schaefer & Strimmer 2005) to our covariance, thus setting a floor on the diagonal elements. The size of the floor should be roughly the same size as the smallest calculated covariance and after some experimentation, we set this value to $10^{-4} \times (N_{\text{QSO}}/10)$, where N_{QSO} is the number of quasars in the data set that is analyzed. We will come back to this subtle point in § 4 when discussing the effects of this floor on our results. Fig. 6 shows the covariance and correlation matrices of the PDF for an ensemble of ten quasar spectra at redshift $z = 3$ generated for a continuum model containing two PCS.

3.5. Effects on the Estimation of γ Due to Continuum Errors and Spectral Noise

We have shown previously that we will have to take continuum errors into account when analyzing the flux PDF's of the normalized quasar spectra. We have also shown how we modify the covariance matrix (§ 3.4) and PDF models (§ 3.2) to include the continuum error due to the intrinsic limitations of the continuum model. We will now demonstrate that these steps are necessary to obtain unbiased estimates of the thermal parameter γ that is our main interest. Note that — in this subsection only — we do not use our full PDF regulated continuum fitting algorithm for illustrating the importance of incorporating the continuum errors, but for the sake of simplicity we conduct an exercise with a simplified version of our method that only estimates the parameter γ and σ_C , but no continuum parameters. Rather we analyze already normalized quasar spectra that have been divided by their best fit continuum model with $N_{\text{PCA}} = 2$ that was estimated when no Ly α forest absorption was added to the spectra (see § 3.1), thus resulting in approximately normalized Ly α forest spectra.

Our MCMC based algorithm produces posterior probability distributions for the free parameters that we would like to estimate, in this particular case only γ and σ_C . We will now examine three different scenarios that we will explain in the following paragraph.

Fig. 7 shows the resulting posterior probability distribution of the parameter γ when running our simplified algorithm for the three different situations for an ensemble of ten quasar spectra. The right and left panel of the figure correspond to the analysis at redshift $z = 3$ and $z = 5$, respectively. The histogram shown in blue represents the first situation which is the ideal case, where there is neither spectral noise nor continuum error, i.e. $\sigma_C = 0$, included in the Ly α forest spectra. Also the PDF models for this ideal case and the covariance matrix assume noise-free spectra without continuum error and thus only contain entries between $0 \leq F \leq 1$. The

covariance matrix used in this case was calculated from multiple PDF's assuming noise-free, perfectly continuum normalized spectra. In this ideal situation our algorithm produces an unbiased estimate for the parameter γ for both redshifts and recovers the fiducial input value of $\gamma = 1.0$ shown as the black vertical line. The posterior probability distribution is not exactly centered around the fiducial value which is due to a random fluctuations in the realization of a finite number of quasar spectra.

Of course this first scenario is very unrealistic, because real quasar spectra contain noise and we do not know their continuum level precisely and hence do not have perfectly normalized Ly α forests. Thus in the second scenario, shown as the yellow histogram, spectral noise and continuum error with $\sigma_C = \sigma_{\text{PCA}=2} \approx 8.4\%$ were added to the Ly α forest spectra by dividing each quasar spectrum by its continuum model with $N_{\text{PCA}} = 2$. However, in the model fitting, we still use the PDF model and the covariance matrix corresponding to the ideal case of noise-free spectra with no continuum error. Thus the PDF of the approximately normalized Ly α forest spectra now contains flux pixels below $f < 0$ and above $f > 1$, but then all pixels outside the flux interval $f \in [0, 1]$ are neglected in the likelihood function. Fig. 7 shows that neglecting the noise and continuum error in the modeling clearly results in a very biased estimate for the parameter γ , with the true fiducial value of $\gamma = 1.0$ lying far outside the resulting posterior probability distribution (yellow histogram).

This example demonstrates the need to incorporate the effects of spectral noise and continuum error into the PDF models and the covariance matrix. Hence we enlarge the range of fluxes that we consider and add these effects as described in § 3.2 and § 3.4 to the models for the PDF and the covariance matrices (for $N_{\text{PCA}} = 2$, i.e. $\sigma_C = \sigma_{\text{PCA}=2} \approx 8.4\%$). We again estimate the posterior distribution for γ , now marginalizing over σ_C as a nuisance parameter. The Ly α forest spectra still contain noise and continuum errors but these effects are now included in the models of the flux PDF and the covariance matrix. The posterior probability distribution for γ in this third scenario is shown in Fig. 7 as the gray histogram. The bias in the γ estimate that arose in the previous case, is now removed, allowing us to recover the fiducial input value, albeit with slightly lower precision than in the idealized first case.

Incorporating continuum error into our PDF models introduced the free parameter σ_C into our formalism. Thus the posterior probability distribution for γ in this last case is marginalized over this parameter. This marginalization and the reduced precision due to spectral noise causes the posterior probability distribution to broaden, which can be seen when comparing the blue and gray histograms. The resulting reduction in precision is greater at $z = 3$, but less obvious at redshift $z = 5$, because continuum errors have a much smaller impact on the PDF models at higher redshift (see Fig. 5). Indeed, the bias that arose in the second scenario when adopting the idealized (noiseless spectra and perfect continuum) models and covariance matrix at redshift $z = 5$, were largely due to the effects of ignoring the noise in modeling, rather than the continuum error.

Fig. 8 shows the PDF models corresponding to the three different scenarios described in Fig. 7. The black

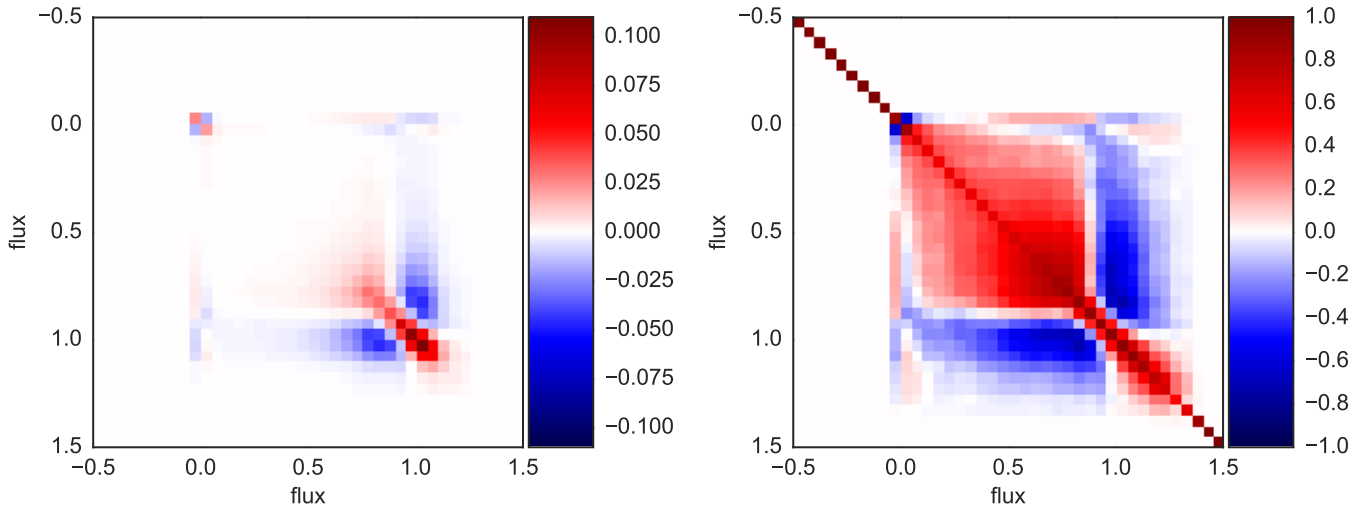


FIG. 6.— Covariance and correlation matrix shown in the left and right panel, respectively. The matrices are created from the PDF’s of ten mock quasar spectra, i.e. $N_{\text{QSO}} = 10$, at redshift $z = 3$ with a fiducial value of $\gamma = 1.0$. Two PCS, i.e. $N_{\text{PCA}} = 2$, are included in the continuum model for normalizing the quasar spectra before calculating the PDF, i.e. the matrices incorporate a continuum error of $\sigma_{\text{PCA}=2} \approx 8.4\%$.

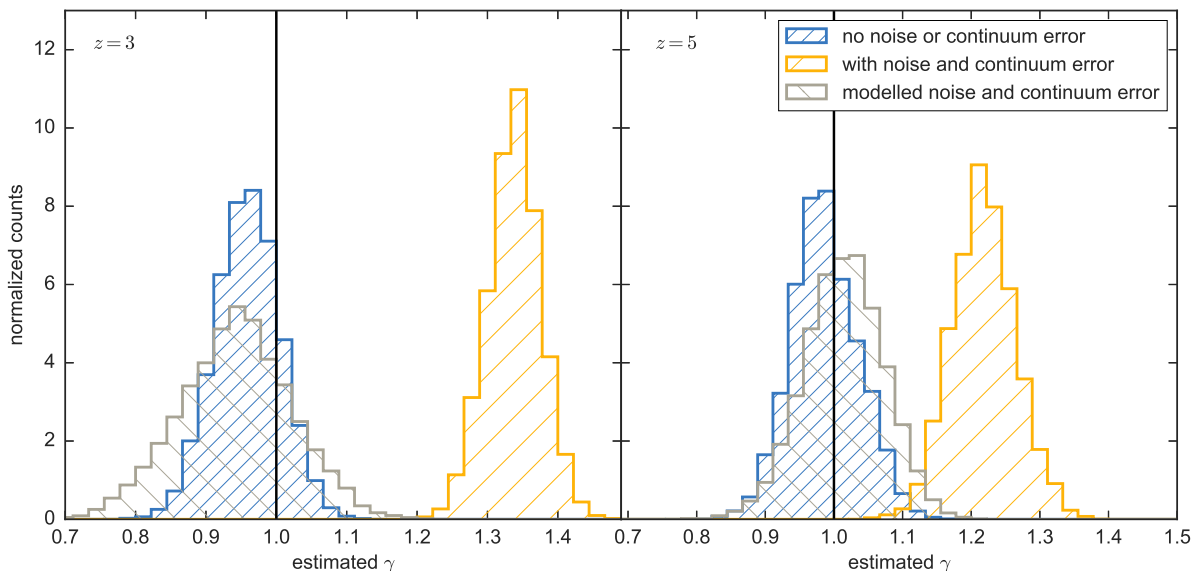


FIG. 7.— Posterior probability distribution of γ for ten realisations of the Ly α forest at redshift $z = 3$ (left panel) and $z = 5$ (right panel). The black vertical line indicates a value of $\gamma = 1.0$, which was used as our fiducial value to generate the quasar data. The blue histogram indicates the posterior probability distribution of γ when assuming a perfectly known continua and noise-free spectra. Introducing continuum errors and spectral noise to the Ly α forest spectra results in a strongly biased distribution (yellow). The gray histogram shows that this bias can be resolved again by modelling the continuum errors and spectral noise into our PDF models and covariance matrices and treating the continuum error σ_C as an additional free parameter that can be estimated and marginalized out.

curves in each panel show the true PDF that ideally should have been recovered by our algorithm, whereas the colored curves show the actual recovered PDF. In the first and third case the recovered PDF models (blue dashed and gray curves) agree with the true PDF models (black curves) very well and lead to an unbiased estimate of the parameter γ (see Fig. 7). The middle panels show the second scenario, where the quasar spectra contain noise and continuum error and thus the resulting PDF’s (yellow curves) contain flux values outside of the considered flux range of $0 \leq f \leq 1$, that is indicated by the black dashed lines. The resulting PDF models

differ from the true PDF models (black curves) and prefer PDF models that correspond to biased values for γ (dotted black curves). Considering a wider range of flux values and modeling the effects of noise and continuum error in the PDF’s and covariance matrices (bottom panels) resolves this discrepancy between the true and the recovered PDF models and the fiducial value of γ can be recovered again.

We now have the tools to obtain unbiased estimates for thermal parameters of the IGM such as γ and can also estimate the uncertainty σ_C inherent to imperfect continuum fits. In the following section we will apply

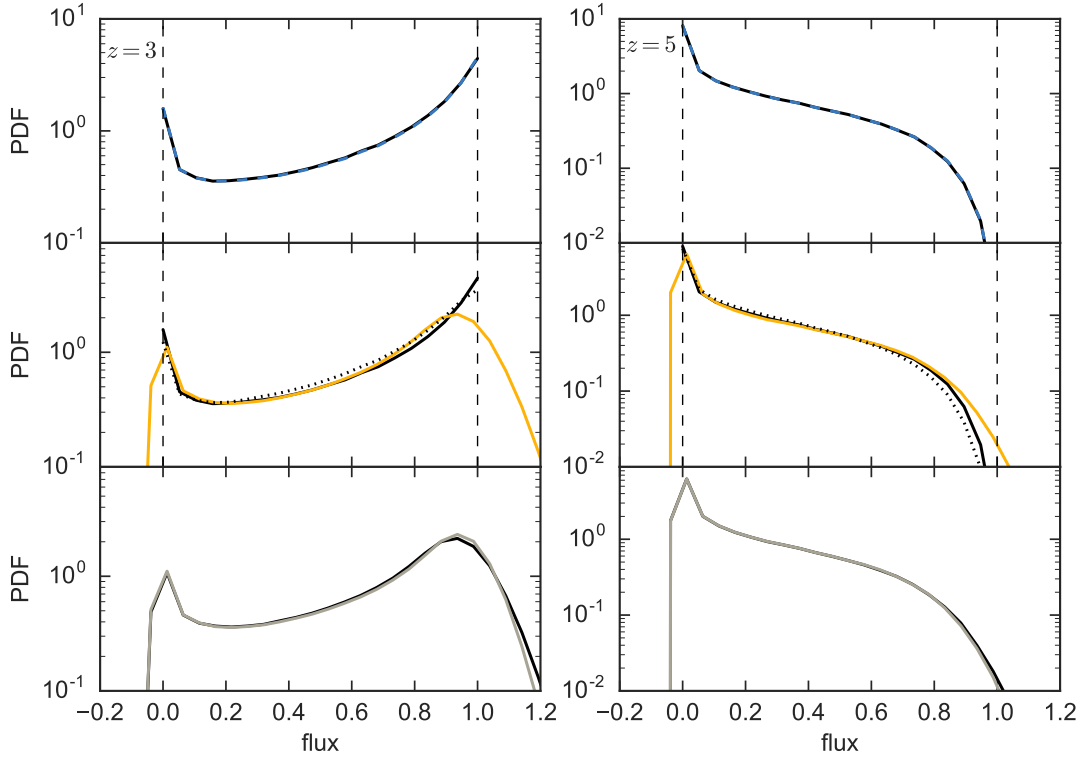


FIG. 8.— Ly α flux PDF’s corresponding to the three described scenarios from Fig. 7 at $z = 3$ (left panels) and $z = 5$ (right panels). *Upper panels:* For noise-free quasar spectra with perfectly known continua our algorithm recovers the true PDF model (black curves) very well, i.e. the recovered PDF models shown as the blue dashed curves and black curves agree. *Middle panels:* Adding noise and the effects of continuum error to the quasar spectra leads to a discrepancy between the true PDF models (black curves) and the recovered PDF models (yellow curves) that rather agree with PDF models that corresponds to a biased value of γ (black dotted curves). The black dashed lines show the considered flux range for estimating the best PDF model. *Bottom panels:* When augmenting the considered flux range in the PDF models and the covariance matrices the recovered PDF models (gray curves) agree again with the true PDF models (black curves) and the fiducial value of γ can be recovered.

our full method to ensembles of mock quasar spectra.

4. RESULTS

In this section we evaluate the efficacy of our new Bayesian formalism for simultaneously estimating the continuum models of an ensemble of quasar spectra, the continuum error, and the thermal properties of the IGM at two different redshifts, $z = 3$ and $z = 5$.

The implicit dependence of the likelihood \mathcal{L}_{PDF} in eqn. (13) on the continuum model parameters α_{ij} arises because each quasar spectrum is divided by its continuum model before the Ly α forest flux PDF can be calculated. The true underlying flux PDF should be the same for an ensemble of quasar spectra at the same redshift, and independent of the continuum parameters. By forcing these quasar spectra to result in the same flux PDF their continua will be regulated by the PDF estimation itself. If one quasar continuum is significantly over- or underestimated the resulting PDF would contain too many low or high flux pixels and the likelihood function \mathcal{L}_{PDF} would disfavor the corresponding PDF model. In this way we have a method to simultaneously estimate the unknown continuum parameters α_{ij} of each quasar, the thermal parameters governing the flux PDF (for our simplified model this is presently only the parameter γ), and the underlying continuum error σ_C . The parameter space thus quickly becomes very large, since for N_{QSO} quasar spectra, each quasar continuum is fit with N_{PCA}

principal components, resulting in a $(N_{\text{QSO}} \times N_{\text{PCA}} + 2)$ -dimensional parameter space. Fig. 9 illustrates the basic idea of our PDF regulated continuum fitting approach. The upper panels show three quasar spectra in black from an ensemble of ten quasar spectra and different estimates of their continua, which are random draws from the posterior probability distributions of the $N_{\text{PCA}} = 2$ continuum model coefficients, where the colors of the curves all indicate the same draw. Note that the continuum models are only fit to the data in between the two gray dashed lines in the region of the Ly α forest between 1040Å and 1190Å. The posterior probability distribution of the continuum model coefficients are obtained via our MCMC based algorithm. The lower panel depicts the resulting PDF’s when normalizing the quasar spectra by their respective continuum models. The black PDF represents the true PDF when assuming the fiducial input parameter of $\gamma = 1.0$ and $\sigma_C = \sigma_{\text{PCA}=2} = 8.4\%$. The colored PDF’s are from the same random draw as the continuum models of the quasar spectra. Note that the PDF’s include the Ly α forest flux pixels from the whole ensemble of ten quasar spectra and not only from the three example spectra shown in the upper panels.

Note that in this paper we consider three different errors. The continuum error that is intrinsic to the continuum model is called σ_{PCA} and is due to the finite number of PCS. The estimated continuum error σ_C is the quantity we estimate with MCMC and want to marginalize

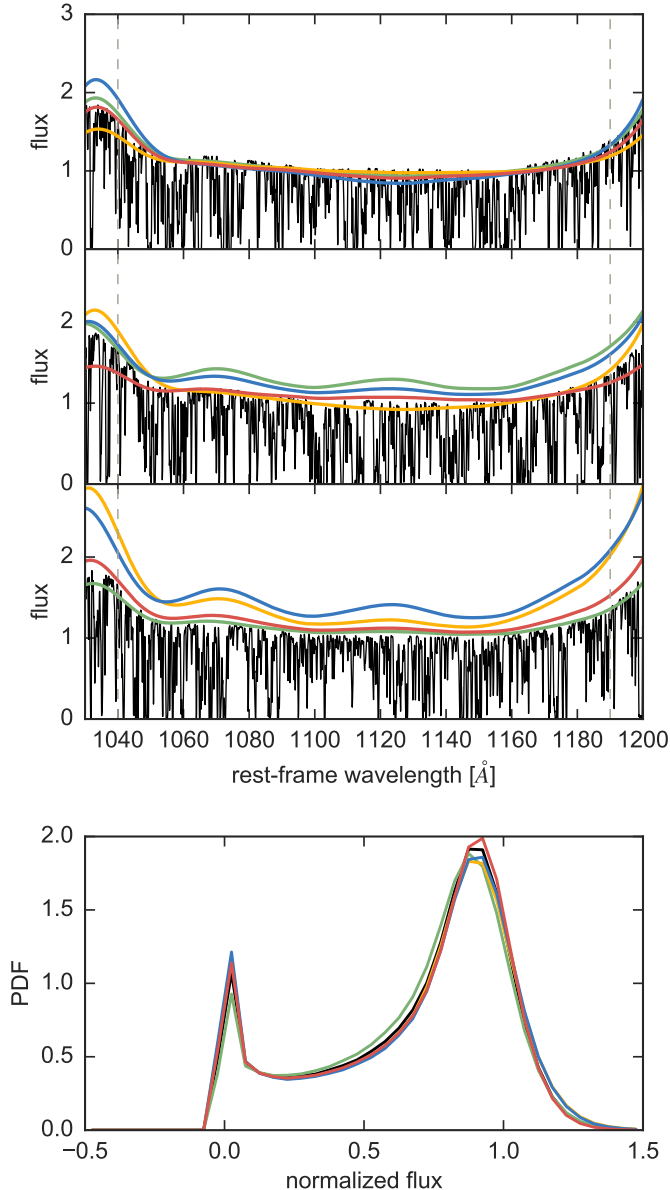


FIG. 9.— The three upper panels show different quasar spectra from the ensemble in black (for better visibility we show the noise-free spectra). The different colored lines show different estimates for their continuum models, estimated in the region between the two gray dashed lines, that indicate the Ly α forest region that we take into account, excluding the effects of proximity zones. The coefficients of the continuum model are random draws from their posterior probability distributions, the different colors representing the same draw. The lower panel shows the corresponding PDF's. The black curve demonstrates the true PDF when assuming the fiducial input parameters. The colored curves show the resulting flux PDF's of the normalized quasar spectra (and the seven other spectra of the ensemble), the colors corresponding to the same random draw from the posterior probability distributions.

out in the end. It is mainly due to the finite precision of the PCS plus it reflects also the inability to precisely determine the continuum in the presence of Ly α absorption. The third error we are considering is the width of the distribution of continuum residuals $\Delta C/C$ (see eqn. (10)), i.e. the actual PDF regulated continuum error $\sigma_{\Delta C/C}$. This gives an estimate of the error between the true quasar continuum and the estimated continuum

model. It can only be calculated when dealing with mock data since we need to know the true quasar continuum. Thus we can test later on whether our estimated continuum error σ_C reflects the actual PDF regulated continuum error $\sigma_{\Delta C/C}$.

First we will investigate how well our algorithm performs on a single ensemble of ten high-resolution quasar spectra, and explore the degeneracies between the parameters that govern the shape of the PDF. We conclude with an assessment of the reliability of our method by applying it to 100 different realizations of ensembles of ten quasar spectra.

4.1. Analysis of an Ensemble of Quasar Spectra

We investigate the efficacy of our algorithm for an ensemble of ten high-resolution quasar spectra, i.e. $N_{\text{QSO}} = 10$, which is a realistic ensemble size corresponding to the path length of a typical redshift bin given current high-resolution spectroscopic quasar samples (Walther et al. in prep.). The continuum models that we analyze have different numbers of PCS, namely $N_{\text{PCA}} = 0, 1, 2, 3, 4$. No principal components $N_{\text{PCA}} = 0$, means that we divide each quasar by the mean quasar spectrum from Suzuki (2006) and only fit for the PDF parameters γ and σ_C . Thus the largest parameter space we are considering corresponds to $N_{\text{QSO}} = 10$ quasar spectra with each continuum modeled with $N_{\text{PCA}} = 4$, which results in a 42-dimensional parameter space. Due to the long computational time that it takes until convergence is achieved, we did not consider continuum models with more components. Also, Fig. 4 shows that we do not expect a big improvement in the precision of the continuum estimation for continuum models with more than 4 PCS.

We show the results for a realization of an ensemble of $N_{\text{QSO}} = 10$ quasar spectra and a continuum model with $N_{\text{PCA}} = 2$ in Fig. 10. We run our MCMC algorithm with 100 walkers for 10,000 steps and chose half the steps as the burn-in time until convergence of the MCMC chains is achieved. The second half of the chains is used as posterior probability distributions. The upper panels show the posterior probability distribution for the parameter γ at redshift $z = 3$ and $z = 5$ in the left and right panel, respectively. In both cases the fiducial input parameter of $\gamma = 1.0$ with which the ensemble of mock quasar spectra was generated, is recovered. The width (i.e. 68%-region) of the posterior probability distribution, which gives the precision with which we can recover γ with this ensemble of ten quasar spectra, is $\pm 8.6\%$ at redshift $z = 3$ and $\pm 6.1\%$ at $z = 5$. Note that we quote the average between the (50th-16th)-percentile and the (84th-50th)-percentile here, since the distributions are fairly symmetric.

The middle panels show the posterior probability distribution of the continuum error σ_C in the estimation of the continuum model of all quasar spectra in the ensemble. At redshift $z = 3$ the ensemble of ten quasar spectra that we chose in this run constrains the continuum error to be $\sigma_C \approx 9.8 \pm 2.1\%$. At redshift $z = 5$ the continuum error σ_C is only mildly constrained. This is not a surprising result given that the flux PDF at this high redshift is fairly insensitive to the level of uncertainty in the continuum estimation (see Fig. 5). In this case the median value of $\sigma_C \approx 12.5 \pm 2.2\%$ should be considered with caution since it will also be dependent on prior assumptions

for σ_C .

The lower panels of Fig. 10 show the actual continuum residuals $\Delta C/C$ for all quasars in the ensemble calculated with eqn. (10), i.e. it shows the relative continuum error between the true quasar continuum and the continuum model estimated via PDF regulation. The obtained median values of $\Delta C/C \approx -2.1\%$ at $z = 3$ and $\Delta C/C \approx -2.8\%$ at $z = 5$ indicate that there is a very small systematic overestimation of the continuum level. The width of this residual distribution, the actual PDF regulated continuum error $\sigma_{\Delta C/C}$, i.e. the average of the (84th-50th) percentile and (50th-16th) percentile, shows that the actual continuum error for this ensemble of ten quasar spectra is $\sigma_{\Delta C/C} \approx 6.7\%$ at $z = 3$ and $\sigma_{\Delta C/C} \approx 10.5\%$ at $z = 5$. These values are slightly lower than the estimated continuum error σ_C , i.e. σ_C is slightly overestimated, but still within the 1σ -region of the posterior probability distribution at $z = 5$ and slightly outside of it (1.46σ) at $z = 3$.

By means of the posterior probability distributions we can explore the degeneracy between the two parameters that govern the shape of the PDF. This is demonstrated in Fig. 11 at redshift $z = 3$ and $z = 5$ in the left and right panel, respectively. The slope parameter γ is shown on the x-axis, versus the continuum error σ_C on the y-axis. The gray dashed lines indicate the fiducial parameter of $\gamma = 1.0$ and the intrinsic error of the continuum model with two PCS, i.e. $\sigma_C = \sigma_{\text{PCA}=2} \approx 8.4\%$ (see Fig. 4).

At redshift $z = 3$ we can obtain constraints for both parameters with our algorithm, since there is no degeneracy between the two parameters of interest. This result can be seen directly in Fig. 1 and Fig. 5, since γ and σ_C alter the shape of the PDF in different manners. At higher redshift at $z = 5$ the constraints on σ_C are very weak, because the PDF of the transmitted flux in the Ly α forest is less sensitive to this parameter as we have seen in Fig. 5. However, at both redshifts we can constrain the slope parameter γ of the temperature-density relation of the IGM, which was our main goal.

4.2. Robustness of the PDF Regulated Continuum Fitting

In this subsection we investigate the robustness and reliability of our method for ensembles of ten high-resolution quasar spectra. Hence we would like to determine whether our method results in possible biases in the model parameters, whether the estimated continuum error σ_C is a good proxy for the actual PDF regulated continuum error $\sigma_{\Delta C/C}$, and how well the continuum error compares to the intrinsic accuracy of the chosen PCA basis. Therefore we run our algorithm a hundred times, each time with a different realization of an ensemble of ten quasar spectra. Each of the 100 runs entails an MCMC, which results in posterior probability distributions for γ and σ_C as well as for the coefficients of the PCS for each quasar. Taking the mean of each posterior probability distribution of the PCS gives us a mean continuum model for each quasar spectrum, which enables us to calculate the continuum residual distribution $\Delta C/C$ and its width, the actual PDF regulated continuum error $\sigma_{\Delta C/C}$.

The results of this investigation are presented in Fig. 12 for redshift $z = 3$ and $z = 5$ in the left and right panels,

respectively. The upper panels show the estimated values for the slope parameter γ of the temperature-density relation as a function of N_{PCA} that were used to model the continuum of each quasar. From each of the hundred runs we obtain a posterior probability distribution for γ and adopt its median as the best estimate (see upper panels of Fig. 10). We then examine this distribution of estimates of γ from the hundred realizations of the quasar ensemble. The data points in the upper panels of Fig. 12 indicate the median of this distribution, i.e. the 50th percentile, and the errorbars show the 16th and 84th percentile. In order to compare to the ideal but unrealistic situation when assuming ensembles of ten noise-free spectra with no continuum error we also show the gray areas that show the median (gray dashed lines) and the 16th to 84th percentile region of estimates of γ . In these cases γ is the only free parameter to estimate with MCMC.

These upper panels of Fig. 12 show that we can recover the thermal parameter γ at both redshifts with an ensemble of ten quasar spectra remarkably well. The medians of the posterior probability distributions for γ are mostly within the 16th to 84th percentile region of the estimates for ensembles of perfect noise-free spectra, and the fiducial input value of $\gamma = 1.0$ lies within the 68%-region of all estimates. For $N_{\text{PCA}} = 2$ which we will adopt as our fiducial model, the median estimate for γ and its 1σ fluctuations at $z = 3$ are $\gamma \approx 1.013$ with $\sigma_\gamma = 8.3\%$ and $\gamma \approx 1.029$ with $\sigma_\gamma = 5.6\%$ at $z = 5$. We expect 1σ -fluctuations around the fiducial value of $\gamma = 1.0$ of $\sigma_{\text{med}\gamma} \approx 8.3\%/\sqrt{100} \approx 0.83\%$ at $z = 3$ ($\sigma_{\text{med}\gamma} \approx 5.6\%/\sqrt{100} \approx 0.56\%$ at $z = 5$) due to the fact that we only investigate 100 different realizations of our ensemble. Hence the estimated values of γ lie marginally outside the expected region. This may be a random fluctuation, however, since the other estimates of γ for different values of N_{PCA} all fluctuate in the same direction it is suggestive that the values are slightly biased. Nevertheless the bias in the estimation of γ is still 6–7 times smaller at $z = 3$ (2–3 times smaller at $z = 5$) than its 1σ errorbars and thus we can tolerate this possible small bias. The marginalization over noise and continuum error leads to a modest reduction of precision in the measurement of γ , since the errorbars increase by a factor of ~ 2 compared to the ideal noise-free case (gray areas).

The middle panels of Fig. 12 illustrate how centered the continuum residuals obtained by PDF regulation are about zero. For each MCMC inference we compute the continuum residuals $\Delta C/C$ in the region of the Ly α forest (i.e. rest-frame wavelengths $1040\text{\AA} \leq \lambda \leq 1190\text{\AA}$) with eqn. (10), and compute the median $\mu_{\Delta C/C}$ of the distribution. This results in a distribution of 100 median values $\mu_{\Delta C/C}$, and the median of this distribution of medians (points), as well as its 16th and 84th percentiles (errorbars), are plotted in the middle panels. The blue dashed lines and shaded regions indicate the corresponding $\mu_{\Delta C/C}$ resulting from errors intrinsic to the PCA continuum model. Specifically, we MCMC fit only the continua of the the same 100 realizations of $N_{\text{QSO}} = 10$ quasars with the PCA model, and performed exactly the same procedure on the resulting $\Delta C/C$ distributions, and 100 $\mu_{\Delta C/C}$ median values.

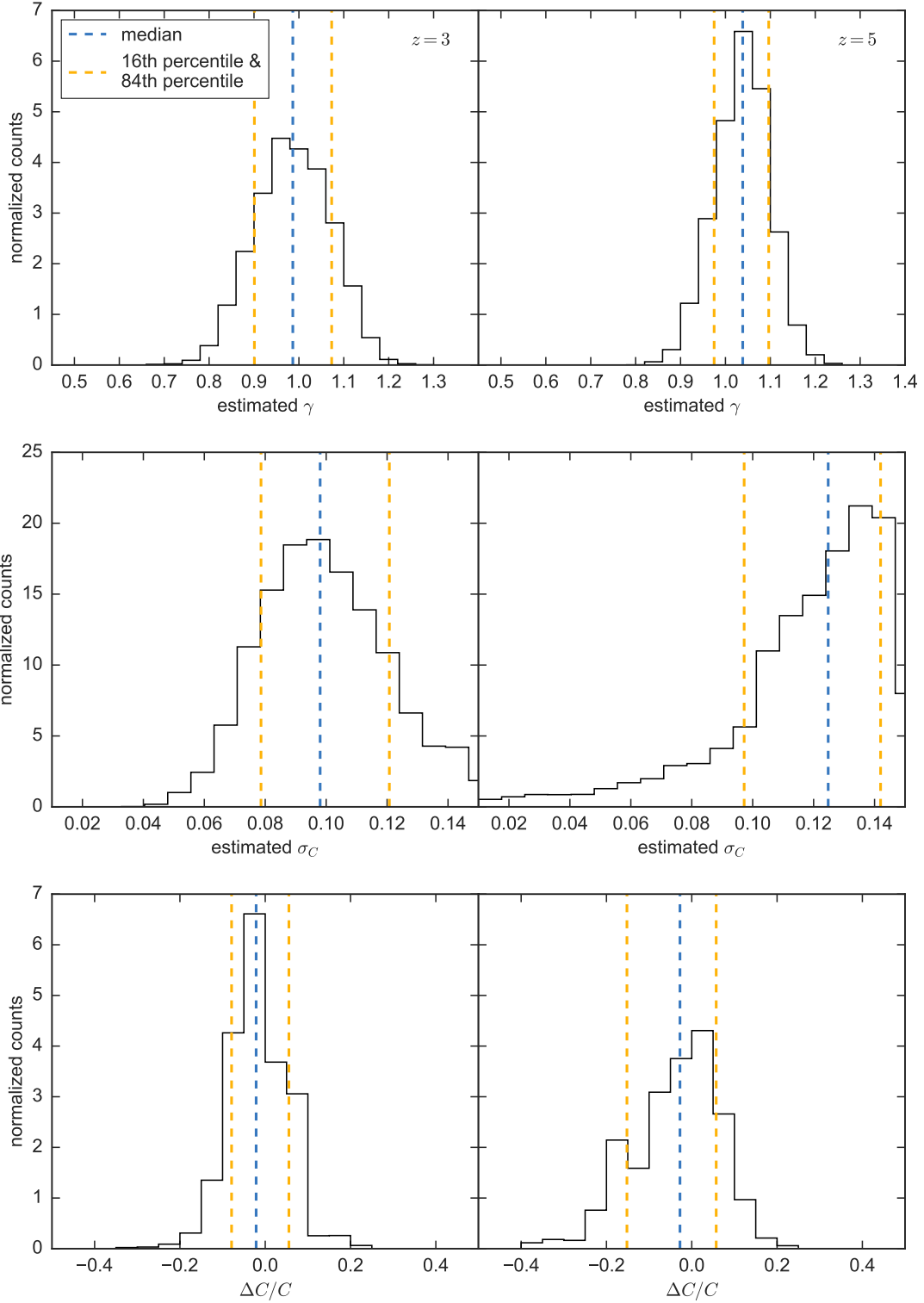


FIG. 10.— Results from our MCMC algorithm for a realization of an ensemble of ten quasar spectra at redshift $z = 3$ (left panels) and redshift $z = 5$ (right panels). *Upper panels:* posterior probability distribution of γ . The blue dashed lines show the median of the posterior probability distributions and the yellow dashed lines represent the 16th and 84th percentiles. *Middle panels:* posterior probability distribution of the estimated continuum error σ_C . *Lower panels:* Distribution of continuum residuals $\Delta C/C$ in the wavelength region of the Ly α forest of all ten spectra of the ensemble.

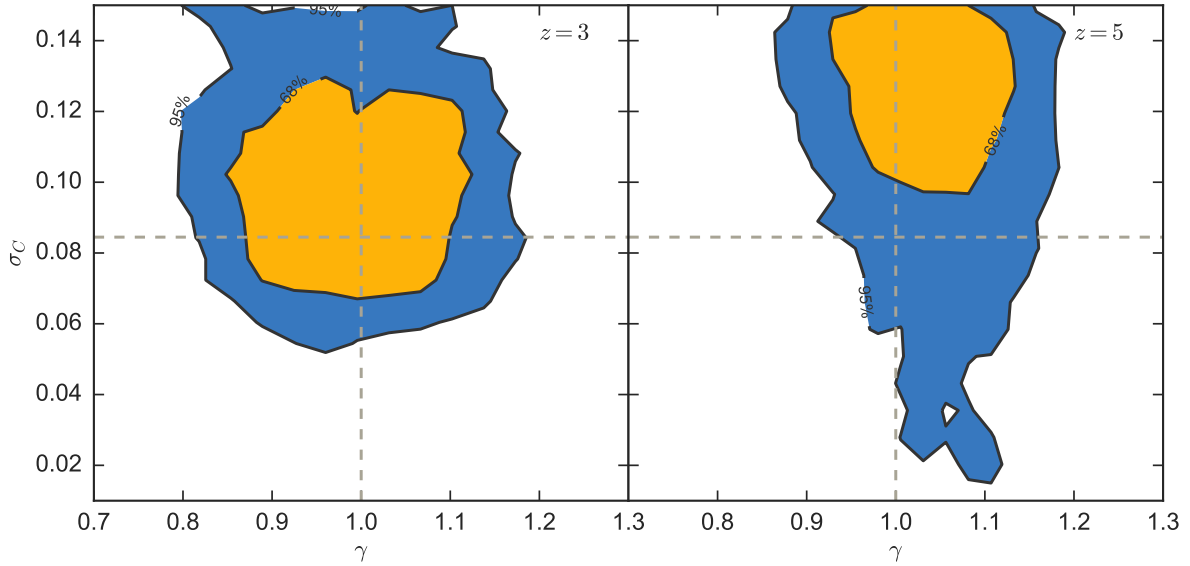


FIG. 11.— Contour plot showing possible degeneracies of the two parameters γ and σ_C for an ensemble of ten quasar spectra at $z = 3$ (left panel) and $z = 5$ (right panel). The gray dashed lines indicate the fiducial input value of $\gamma = 1.0$ and the continuum error $\sigma_{\text{PCA}=2} \approx 8.4\%$ that is intrinsic to the continuum model with two PCS.

A completely unbiased continuum estimation would give a continuum residual distribution with a median of $\mu_{\Delta C/C} \approx 0$. We see that both at $z = 3$ and at $z = 5$, there is a small negative bias of a few percent in the estimates, i.e. we slightly overestimate the quasar continuum level. However, this bias is below 2% at $z = 3$ and below 3% at $z = 5$ for $N_{\text{PCA}} = 4$ and even smaller for $N_{\text{PCA}} < 4$, and thus insignificant relative to the typical continuum residuals $\Delta C/C$ of $\sim 7 - 10\%$ (lower panel Fig. 10). For $N_{\text{PCA}} = 2$, which represents our fiducial model, our algorithm overestimates the continuum by $\approx 1.5\%$ at $z = 3$ and $\approx 2.4\%$ at $z = 5$. Our measured $\mu_{\Delta C/C}$ are marginally consistent, i.e. the 68%-regions overlap, with the continuum residuals intrinsic to the continuum model, i.e. the shaded blue regions. For $N_{\text{PCA}} \geq 2$ our PDF regulated continuum fits are just slightly more biased than the one obtained by fitting the PCA model to the quasar spectra in the absence of Ly α forest. However, the biases we obtain are much smaller than those estimated for hand-fitted quasar continua (see e.g. Faucher-Giguère et al. 2008).

The lower panels of Fig. 12 illustrate the behavior of the 1σ error of our continuum estimates. Recall that we characterize continuum errors in two different ways: once we fit for the continuum error σ_C and obtain an estimate via MCMC; in the other case we calculate the continuum residuals $\Delta C/C$ using our knowledge of the true continua of the mock spectra, and take the width of this distribution $\sigma_{\Delta C/C}$ as the estimate for the continuum error. The black points with error bars represent the median and the 16th and 84th percentiles of the inferred continuum error σ_C from our MCMC PDF continuum regulation. Specifically, for each of the 100 realizations of ten quasar spectra, we performed MCMC PDF regulation, obtained a posterior probability distribution for σ_C and adopted its median value as the best estimate. This results in 100 median σ_C values, where the median and the 16th and 84th percentiles (errorbars) are shown in black. The blue data points correspond to the actual PDF regulated continuum error, i.e. the measured dispersion $\sigma_{\Delta C/C}$ of the continuum residuals $\Delta C/C$. For each run we compute the continuum residuals $\Delta C/C$ for all pixels for the whole ensemble of quasars and take the average of the 16th and 84th percentile of this distribution as the estimate for $\sigma_{\Delta C/C}$. We obtain 100 of these measurements for each realization of the quasar ensemble and plot the median value and the 16th and 84th percentiles. The blue shaded areas show the same distributions of median values for the ideal case with the noise-free spectra and no Ly α forest, i.e. the error intrinsic to the continuum model for a given N_{PCA} ⁶.

Comparing the actual error of the PDF regulated continuum residuals (blue points) with the intrinsic precision of the PCA basis (blue shaded region) in the lower left panel at $z = 3$, one sees that our algorithm recovers the continuum consistent with the best accuracy achiev-

able with the PCA basis, at least for $N_{\text{PCA}} \leq 2$. For higher values of $N_{\text{PCA}} > 2$ the blue points lie slightly above the intrinsic accuracy of the PCA model shown by the shaded regions, and thus our PDF regulated continuum fits perform slightly worse than the underlying PCA model. One might expect the PDF regulated continuum error (blue points) to continue to decrease as N_{PCA} is increased, following the intrinsic error of the PCA basis (shaded region), but instead the PDF regulated continuum errors saturate around a value of $\sigma_{\Delta C/C} = 0.07$. We believe that this is due to the floor that we introduced into our covariance matrix (see § 3.4) in order to prevent it from becoming singular. This floor sets a threshold below which we can no longer measure continuum errors. Once the chosen PCA basis gets accurate enough, we can no longer recover the small continuum errors, since the floor reduces the sensitivity particularly in the high flux bins of the PDF, which are most sensitive to the continuum error (see Fig. 5).

Our results at $z = 5$ in the lower right panel of Fig. 12 tell a similar story. The PDF regulated continuum error (blue points) do not follow the intrinsic error of the PCA basis (shaded region) for $N_{\text{PCA}} \geq 2$. This most likely results from the reduced sensitivity of the PDF at $z = 5$ to the continuum (see Fig. 5), and possibly also due to the floor we imposed in the covariance matrix.

A comparison between the black data points showing the inferred continuum error σ_C and the blue data points indicating the PDF regulated continuum error $\sigma_{\Delta C/C}$ at $z = 3$ reveals that our algorithm gives a fairly good estimate for the actual continuum error. Nevertheless the inferred values are slightly biased. We underestimate the continuum error for $N_{\text{PCA}} = 0$ and $N_{\text{PCA}} = 1$ and slightly overestimate it for $N_{\text{PCA}} \geq 2$. However, the inferred values of σ_C usually lie within the 16th and 84th percentile region of the real measured value $\sigma_{\Delta C/C}$. The errorbars on the σ_C estimates are very small indicating that the MCMC always converges to the same range of values. We believe that this is also an artifact resulting from the floor imposed on our covariance matrix.

At redshift $z = 5$ the algorithm seems to recover the actual continuum error better, i.e. the inferred continuum error σ_C (black data points) and real measured PDF regulated continuum error $\sigma_{\Delta C/C}$ (blue data points) agree fairly well, but since the locations of the black inferred values are not well constrained because the posterior probability distributions for σ_C is fairly flat (see middle right panel of Fig. 10), this agreement is partly coincidental and dependent on our choice of the prior probability distribution on σ_C in the MCMC.

In summary, the lower panel of Fig. 12 illustrates that our PDF regulated continuum fitting method is producing continuum errors at $z = 3$ that roughly track the intrinsic precision of the PCA basis, since both the actual PDF regulated continuum error $\sigma_{\Delta C/C}$ (blue points) as well as the inferred continuum error σ_C (black points) lie within the blue shaded region for $N_{\text{PCA}} \leq 2$. At redshift $z = 5$ the inferred continuum uncertainties are only weakly constrained but nevertheless reliable.

How many PCS should be used? At $z = 3$, the lower left panel shows a drop in the continuum error in both the inferred continuum error σ_C and the real measured continuum error $\sigma_{\Delta C/C}$ and thus an increase of the preci-

⁶ This corresponds to the lower panel of Fig. 4 with the difference being that for the previous plot we calculate the width of the continuum residuals for all 50 HST quasars, whereas in Fig. 12 we show the distribution of median values of the widths of the continuum residuals from each ensemble of ten quasars. Thus the blue dashed lines in Fig. 12 and the data points in the lower panel of Fig. 4 do not agree exactly but differ slightly due to random noise fluctuations.

sion in the continuum model when two or more principal components are taken into account. At redshift $z = 5$ the drop in the continuum error is small, which is due to the fact that the PDF at this redshift barely constrains the quasar continuum level as we have seen before in Fig. 5. At both redshifts the gains in precision for more N_{PCA} , i.e. $N_{\text{PCA}} = 3$ or $N_{\text{PCA}} = 4$, is insignificant. Since we are only interested in the continuum residuals in the wavelength region of the Ly α forest, only the PCS that alter the shape of the quasar continuum in this region are influential for our method. The first principal component spectrum for example mainly addresses the shape of the Ly α emission line, and hence does not improve the continuum estimation in the Ly α forest region. This is why the continuum error is not reduced before taking at least two PCS, i.e. $N_{\text{PCA}} \geq 2$, in the continuum model.

Thus we advocate using the continuum model with two PCS for this analysis, since we want to minimize the number of free parameters and thus the dimensionality of our parameter space which in turn limits the computational time. This implies that we have two nuisance parameters for the continuum estimation per quasar plus the global parameters that influence the shape of the PDF — σ_C and any parameters related to the physics of the IGM, which for our simplified IGM model is only γ . For an ensemble of ten quasar spectra this results in a $2 \times N_{\text{QSO}} + 2 = 22$ dimensional parameter space. However, in principle our method can accommodate larger ensembles of quasar spectra and a more complicated model of the IGM.

5. DISCUSSION AND CAVEATS

In this section we will discuss several caveats of our algorithm and possibilities for further development that will be subject to future work.

5.1. Enlarging the Parameter Space

Although this study only considered a highly simplified single parameter model of the thermal state of the IGM, in practice our method can easily accommodate a more complicated multi-parameter PDF model, the only limitations being computational time and effort. When applying this method to real quasar spectra one would use hydrodynamical simulations to generate the IGM model and also consider the temperature at mean density T_0 , the Jeans pressure smoothing scale λ_P (Rorai et al. 2013; Kulkarni et al. 2015), and other possible nuisance parameters (Lee et al. 2015). Adding more thermal parameters or other nuisance parameters related to the IGM (e.g. Lyman Limit Systems) extends the computational effort only marginally. More parameters in the continuum model on the other hand, add a more significant amount of time to the computation because they need to be estimated for each quasar in the ensemble and hence the number of continuum parameters multiplies with N_{QSO} . In this work we compressed the continuum error of each quasar spectra into only two nuisance parameters. We tested our algorithm with an ensemble of ten quasar spectra, but a larger ensemble with even double the number of quasar spectra is still easily feasible. A larger ensemble of quasar spectra would also further improve the precision on our estimates of the thermal parameters.

5.2. Fixing the Mean Flux

The mean flux of the Ly α forest has been held fixed in our analysis. Therefore, we computed a hundred different realizations of the Ly α forest for each value of γ that we considered in our models and computed a scaling factor for the optical depth τ averaged over the hundred Ly α realizations, in order to match the mean flux in our mock spectra to measurements of the mean flux (see § 2.1). While creating each mock quasar spectrum we re-scale τ with the scaling factor. In this way, the average mean flux of the Ly α forest is kept fixed, but individual mock spectra can have higher or lower mean flux values, which is expected to be the case also for real quasar spectra due to cosmic variance.

The mean flux could be considered as an additional nuisance parameter in the PDF models. This would not add significantly to the computation time (see § 5.1), but might decrease the precision of the thermal parameter estimation slightly. However, given the precision of the most recent mean flux measurements ($\Delta\langle f \rangle_{z \sim 3} \approx 1\%$ and $\Delta\langle f \rangle_{z \sim 5} \approx 7\%$ Becker et al. (2013)), we opted to keep it fixed.

5.3. Redshift Evolution in the Ly α Forest

In our simplified model for Ly α forest absorption we do not take the redshift evolution within the Ly α forest along the line of sight into account, i.e. we assume a fixed value of γ . However, assuming a redshift evolution within the Ly α forest and thus within the temperature-density relation of the IGM, would result into a redshift dependent slope parameter, i.e. $\gamma(z)$. Our parameter space of the PDF models can be easily augmented with a redshift dependent γ and we would only need to account for one more free parameter in the MCMC runs.

Rorai et al. (2016) discuss temperature-density relations with a break in the slope, i.e. a different slope for over- or underdensities. Even such non-linear dependencies can be easily accommodated in our algorithm by simply constructing a different set of PDF models that contain two different linear slope parameter γ . These models can be parameterized by two parameters γ_o and γ_u for over- and underdense regions, respectively, which simply adds another free parameter to our algorithm.

In principle the PDF models can be made arbitrarily complicated by adding more and more nuisance parameters that will be marginalized out in the end.

5.4. The Choice of the PCA Basis

A more suitable set of PCS could further increase the precision of the continuum model and reduce the continuum error without increasing the number of free parameters in the continuum model and thus the computational time. The PCS that we use in this work from Suzuki (2006) cover the the whole spectral range from 1020Å-1600Å of quasar spectra. However, for the studies of the IGM, one is interested in a small range of wavelengths, i.e. the spectral range spanning the Ly α forest. Thus some of the PCS we use account for the different shapes in the Ly α and other emission lines for example, but do not help improve the continuum model in the Ly α forest region. One could thus come up with a different PCA basis that would be more suited for our purposes. Other methods, such as an Independent Component Analysis (e.g. Allen et al. 2011) or Heteroscedastic Matrix Factor-

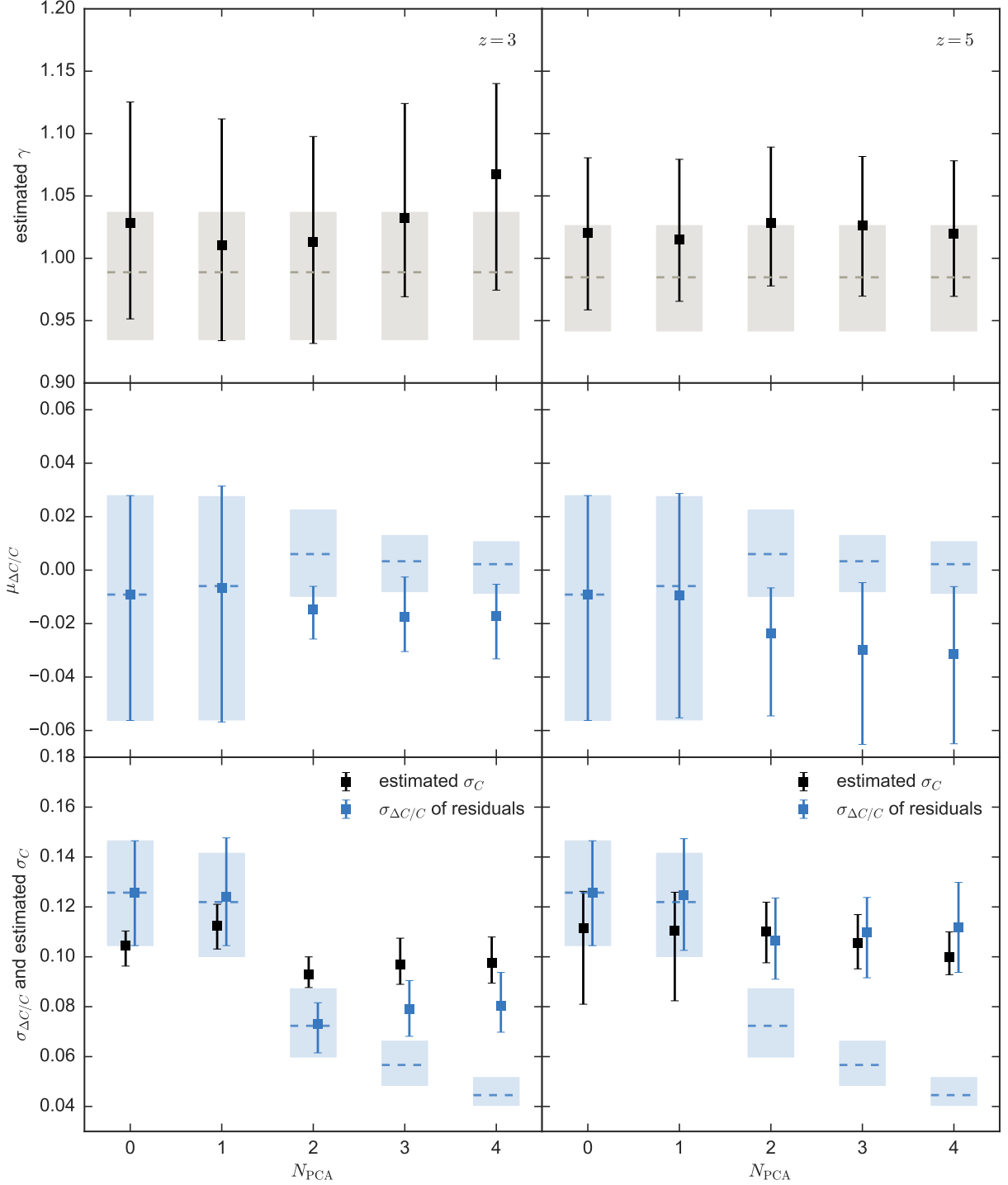


FIG. 12.— Estimated values for γ (upper panels), the continuum residuals (middle panels) and the continuum error (lower panels) dependent on the number of PCS that were taken into account to model each quasar continuum at redshift $z = 3$ (left panels) and redshift $z = 5$ (right panels). Shown are the median and 16th and 84th percentiles. *Upper panels:* distribution of estimates for γ with gray shaded areas showing the ideal distribution of estimates for γ when noise-free quasar spectra and perfect knowledge of the quasar continua are assumed. Note that the fiducial value is $\gamma = 1.0$, but since we only take 100 realizations the distribution fluctuates around this fiducial value. In this case γ is the only free parameter to estimate from the ensemble. For each data point we run our algorithm a hundred times with a different realisation of the ensemble of ten quasar spectra and plot the distribution of the median values of the posterior probability distributions. *Middle panels:* distribution of medians of the continuum residual distribution in the Ly α forest region. The blue shaded areas show the continuum residual distribution intrinsic to the continuum models. *Lower panels:* showing the continuum errors; the blue data points indicate the real measured widths $\sigma_{\Delta C/C}$ of the continuum residuals whereas the black data points show the distribution of median estimates of the inferred continuum error σ_C . The blue shaded areas show the intrinsic error of the continuum model due to the limited number of principal components.

ization (e.g. Tsalmantza & Hogg 2012), could also be useful to construct a more suitable continuum model while keeping the dimensionality of the PCA low.

Once applying this algorithm to real quasar spectra, the chosen set of PCS might not be flexible enough to account for enough of the variance in the spectra. However, for high- z spectra, the PCA basis of Pâris et al. (2011) could be applied for instance, or a new set of PCA could be created from a similar procedure by fitting the $> 10,000$ spectra available with high S/N ratio in the BOSS survey. If such an augmented and improved PCA were constructed and fit to real data, if the red side of each spectrum is modeled well by the PCA, there is no reason to believe that the blue side is not expected to match.

5.5. Construction of Covariance Matrices

We used an approximation when constructing the covariance matrix, whereby we fixed the covariance matrix to have the intrinsic continuum error of a single continuum model. This fact required us to add a floor to the covariance matrix according to the matrix shrinkage approach, in order to prevent the matrix from becoming singular, since the very high and very low flux bins were rarely populated for the fiducial model used to construct the covariance. This approximation set a floor on the accuracy of our PDF regulated continuum, and limited our ability to obtain more precise continuum fits by increasing the number of PCS. Thus in the future it would be worthwhile to construct covariance matrices as a function of the model parameters γ , σ_C and possible others. This would remove the bias in the continuum residuals and increase the precision of the continuum estimation. However, constructing covariance matrices with varying σ_C is tricky, since we introduced the continuum error into our PDF models by construction without any covariance (eqn. (11)). One possible approach to solve this problem could be to interpolate between the covariance matrices with continuum errors intrinsic to the chosen continuum model. This will be the subject of future work.

5.6. Flux Calibration of the Quasar Spectra

Applying our new algorithm to real quasar spectra requires the spectra to be flux calibrated. Suzuki et al. (2003) showed how one can flux calibrate Echelle spectra using lower resolution spectra with accurate spectrophotometry. We do not expect any problems arising due to errors and uncertainties on this flux calibration, since we infer the continuum error σ_C with MCMC, and any flux calibration errors would become a part of the continuum error that we can marginalize out.

6. SUMMARY AND CONCLUSION

We presented a new Bayesian algorithm making use of MCMC sampling that allows us to simultaneously estimate the unknown continuum level of each quasar in an ensemble of high-resolution spectra as well as their common Ly α forest flux PDF. This fully automated PDF regulated continuum fitting method models the unknown quasar continuum with a PCA basis with the coefficients of the principal components treated as nuisance parameters. This method allows us to estimate parameters governing the thermal state of the IGM, such as the slope

of the temperature-density relation, while marginalizing out continuum uncertainties in a fully Bayesian way.

The primary results of this study are:

- The intrinsic error in the model for the quasar continuum due to a finite number of PCS has a significant impact on the shape of the PDF of the transmitted flux in the Ly α forest at $z = 3$, whereas the Ly α flux PDF at higher redshifts of $z = 5$ is mostly unaffected by the continuum error.
- We incorporate the continuum error and Gaussian white noise into the models for the PDF and into the covariance matrices and show that by treating these effects as nuisance parameters and marginalizing out the continuum error and noise our algorithm removes any biases in the estimation of the thermal parameters.
- We show that our algorithm recovers γ , the only thermal parameter we consider in a simplified model of the IGM, without a significant bias and with high precision for an ensemble of ten high-resolution quasar spectra. We obtain a precision of $\pm 8.6\%$ at $z = 3$ and $\pm 6.1\%$ at $z = 5$ marginalized over all uncertainties in the continuum estimation.
- We explore the degeneracy between the two free parameters of our PDF models, the thermal parameter γ and the model dependent parameter for the continuum error σ_C . As expected we do not see strong degeneracies since both parameters alter the shape of the PDF in slightly different ways. At $z = 5$ the constraints on σ_C are very weak as we expect from the insensitivity of the PDF to this parameter at high redshifts.
- We advocate using $N_{\text{PCA}} = 2$ for modeling each quasar continuum since it minimizes the number of continuum parameters without significant loss in precision when determining thermal parameters or the quasar continua.
- The PDF regulated continuum achieves a precision of $\sigma_{\Delta C/C} \approx 6.7\%$ at $z = 3$, which is in agreement with the intrinsic precision of the continuum model. At $z = 5$ given the limited sensitivity of the Ly α flux PDF, we cannot quite recover the intrinsic precision of the continuum model. The PDF regulated continuum at $z = 5$ has an error of $\sigma_{\Delta C/C} \approx 10.5\%$.
- At $z = 3$ we show that our estimated continuum error σ_C for an ensemble of ten quasar spectra tracks the underlying real measured continuum error fairly well for $N_{\text{PCA}} \leq 2$. At $z = 5$ the PDF of the Ly α forest flux is only slightly dependent on the continuum estimation and thus we only obtain mild constraints for the continuum error σ_C that nevertheless give a rough estimate of the actual underlying continuum error.
- The distribution of continuum residuals shows that the quasar continua are generally slightly overestimated by $\mu_{\Delta C/C} \approx 1.5\%$ at $z = 3$ and $\mu_{\Delta C/C} \approx 2.4\%$ at $z = 5$ for a continuum model with $N_{\text{PCA}} = 2$.

Our algorithm improves upon previous work in two important ways. First, the method is totally automated and thus avoids tedious manual fitting of the quasar continua. Fitting quasar continua by hand could result in continuum errors that are correlated with flux and dependent on the underlying IGM model (Lee 2012), which results in systematic errors that are very difficult to model. Secondly, we model the errors due to imprecise continuum fits and treat them as a nuisance parameter. This results in unbiased estimates of the thermal parameters that are our primary interest, with all continuum uncertainties marginalized out in a Bayesian way. Given

the large amount of high-resolution and high S/N quasar data now publicly available (Lehner et al. 2014; O’Meara et al. 2015), the time is ripe to apply this new methodology to real data.

ACKNOWLEDGMENT

We thank Alberto Rorai, David W. Hogg and the members of the ENIGMA group⁷ at the Max Planck Institute for Astronomy (MPIA) for helpful discussions.

We would also like to thank the referee for his helpful and thorough comments that significantly improved this paper.

REFERENCES

- Allen, J. T., Hewett, P. C., Maddox, N., Richards, G. T., & Belokurov, V. 2011, *Monthly Notices of the Royal Astronomical Society*, 410, 860
- Almgren, A. S., Bell, J. B., Lijewski, M. J., Lukić, Z., & Van Andel, E. 2013, *Astrophysical Journal*, 765, 39
- Bechtold, J., Dobrzycki, A., Wilden, B., et al. 2002, *VizieR Online Data Catalog*, 214, 143
- Becker, G. D., Bolton, J. S., & Lidz, A. 2015, ArXiv e-prints, arXiv:1510.03368
- Becker, G. D., Hewett, P. C., Worseck, G., & Prochaska, J. X. 2013, *Monthly Notices of the Royal Astronomical Society*, 430, 2067
- Becker, G. D., Rauch, M., & Sargent, W. L. W. 2007, *Astrophysical Journal*, 662, 72
- Bi, H., & Davidsen, A. F. 1997, *Astrophysical Journal*, 479, 523
- Bi, H. G., Boerner, G., & Chu, Y. 1992, *Astronomy and Astrophysics*, 266, 1
- Bolton, J. S., Becker, G. D., Haehnelt, M. G., & Viel, M. 2014, *Monthly Notices of the Royal Astronomical Society*, 438, 2499
- Bolton, J. S., Viel, M., Kim, T.-S., Haehnelt, M. G., & Carswell, R. F. 2008, *Monthly Notices of the Royal Astronomical Society*, 386, 1131
- Broderick, A. E., Chang, P., & Pfrommer, C. 2012, *Astrophysical Journal*, 752, 22
- Calura, F., Tesconi, E., D’Odorico, V., et al. 2012, *Monthly Notices of the Royal Astronomical Society*, 422, 3019
- Calverley, A. P., Becker, G. D., Haehnelt, M. G., & Bolton, J. S. 2011, *Monthly Notices of the Royal Astronomical Society*, 412, 2543
- Cen, R., Miralda-Escudé, J., Ostriker, J. P., & Rauch, M. 1994, *Astrophysical Journal Letters*, 437, L9
- Chang, P., Broderick, A. E., & Pfrommer, C. 2012, *Astrophysical Journal*, 752, 23
- Compostella, M., Cantalupo, S., & Porciani, C. 2013, *Monthly Notices of the Royal Astronomical Society*, 435, 3169
- Croft, R. A. C., Weinberg, D. H., Katz, N., & Hernquist, L. 1998, *Astrophysical Journal*, 495, 44
- Croft, R. A. C., Weinberg, D. H., Pettini, M., Hernquist, L., & Katz, N. 1999, *Astrophysical Journal*, 520, 1
- Dall’Aglio, A., Wisotzki, L., & Worseck, G. 2008, *Astronomy and Astrophysics*, 491, 465
- Davé, R., Hernquist, L., Katz, N., & Weinberg, D. H. 1999, *Astrophysical Journal*, 511, 521
- Desjacques, V., Nusser, A., & Sheth, R. K. 2007, *Monthly Notices of the Royal Astronomical Society*, 374, 206
- Faucher-Giguère, C.-A., Prochaska, J. X., Lidz, A., Hernquist, L., & Zaldarriaga, M. 2008, *Astrophysical Journal*, 681, 831
- Foreman-Mackey, D., Hogg, D. W., Lang, D., & Goodman, J. 2013, *Publications of the Astronomical Society of the Pacific*, 125, 306
- Furlanetto, S. R., & Oh, S. P. 2008, *The Astrophysical Journal*, 682, 14
- Garzilli, A., Bolton, J. S., Kim, T.-S., Leach, S., & Viel, M. 2012, *Monthly Notices of the Royal Astronomical Society*, 424, 1723
- Gnedin, N. Y., & Hui, L. 1998, *MNRAS*, 296, 44
- Goodman, J., & Weare, J. 2010, *Communications in Applied Mathematics and Computational Science*, 5
- Hui, L., & Gnedin, N. Y. 1997, *Monthly Notices of the Royal Astronomical Society*, 292, 27
- Hui, L., & Haiman, Z. 2003, *Astrophysical Journal*, 596, 9
- Jenkins, E. B., & Ostriker, J. P. 1991, *Astrophysical Journal*, 376, 33
- Kim, T.-S., Bolton, J. S., Viel, M., Haehnelt, M. G., & Carswell, R. F. 2007, *Monthly Notices of the Royal Astronomical Society*, 382, 1657
- Kulkarni, G., Hennawi, J. F., Oñorbe, J., Rorai, A., & Springel, V. 2015, *Astrophysical Journal Letters*, 812, 30
- Lee, K.-G. 2012, *The Astrophysical Journal*, 753, 136
- Lee, K.-G., Suzuki, N., & Spergel, D. N. 2012, *The Astrophysical Journal*, 143, 51
- Lee, K.-G., Hennawi, J. F., Spergel, D. N., et al. 2015, *Astrophysical Journal*, 799, 196
- Lehner, N., O’Meara, J. M., Fox, A. J., et al. 2014, *The Astrophysical Journal*, 788, 119
- Lidz, A., Faucher-Giguère, C.-A., Dall’Aglio, A., et al. 2010, *The Astrophysical Journal*, 718, 199
- McDonald, P., Miralda-Escudé, J., Rauch, M., et al. 2001, *The Astrophysical Journal*, 562, 52
- . 2000, *The Astrophysical Journal*, 543, 1
- McDonald, P., Seljak, U., Burles, S., et al. 2006, *The Astrophysical Journal Supplement Series*, 163, 80
- McQuinn, M. 2015, ArXiv e-prints, arXiv:1512.00086
- McQuinn, M., Lidz, A., Zaldarriaga, M., et al. 2009, *Astrophysical Journal*, 694, 842
- McQuinn, M., & Upton Sanderbeck, P. 2015, ArXiv e-prints, arXiv:1505.07875
- Meiksin, A., & Tittley, E. R. 2012, *Monthly Notices of the Royal Astronomical Society*, 423, 7
- Meiksin, A. A. 2009, *Reviews of Modern Physics*, 81, 1405
- Miralda-Escudé, J., Cen, R., Ostriker, J. P., & Rauch, M. 1996, *The Astrophysical Journal*, 471, 582
- Mortlock, D. J. 2015, ArXiv e-prints, arXiv:1511.01107
- Oñorbe, J., Hennawi, J. F., & Lukić, Z. 2016, ArXiv e-prints, arXiv:1607.04218
- O’Meara, J. M., Lehner, N., Howk, J. C., et al. 2015, *The Astrophysical Journal*, 150, 111
- Pâris, I., Petitjean, P., Rollinde, E., et al. 2011, *Astronomy & Astrophysics*, 530, A50
- Pfrommer, C., Chang, P., & Broderick, A. E. 2012, *Astrophysical Journal*, 752, 24
- Puchwein, E., Pfrommer, C., Springel, V., Broderick, A. E., & Chang, P. 2012, *Monthly Notices of the Royal Astronomical Society*, 423, 149
- Rollinde, E., Theuns, T., Schaye, J., Pâris, I., & Petitjean, P. 2013, *Monthly Notices of the Royal Astronomical Society*, 428, 540
- Rorai, A., Hennawi, J. F., & White, M. 2013, *Astrophysical Journal*, 775, 81
- Rorai, A., Becker, G. D., Haehnelt, M. G., et al. 2016, ArXiv e-prints, arXiv:1611.03805
- Rudie, G. C., Steidel, C. C., & Pettini, M. 2012, *The Astrophysical Journal Letters*, 757, L30
- Schaefer, J., & Strimmer, K. 2005, *Statistical Applications in Genetics and Molecular Biology*, 4
- Schaye, J., Theuns, T., Rauch, M., Efstathiou, G., & Sargent, W. L. W. 2000, *Monthly Notices of the Royal Astronomical Society*, 318, 817
- Suzuki, N. 2006, *The Astrophysical Journal Supplement Series*, 163, 110
- Suzuki, N., Tytler, D., Kirkman, D., O’Meara, J. M., & Lubin, D. 2003, *The Publications of the Astronomical Society of the Pacific*, 115, 1050
- . 2005, *The Astrophysical Journal*, 618, 592
- Theuns, T., & Zaroubi, S. 2000, *Monthly Notices of the Royal Astronomical Society*, 317, 989
- Tsalmantza, P., & Hogg, D. W. 2012, *The Astrophysical Journal*, 753, 122
- Viel, M., Bolton, J. S., & Haehnelt, M. G. 2009, *Monthly Notices of the Royal Astronomical Society*, 399, L39
- Walther, M., Lee, K.-G., & Hennawi, J. F. in prep.

⁷ <http://www.mpia-hd.mpg.de/ENIGMA/>

Weinberg, D. H., Davé, R., Katz, N., & Kollmeier, J. A. 2003, in American Institute of Physics Conference Series, Vol. 666, The Emergence of Cosmic Structure, ed. S. H. Holt & C. S. Reynolds, 157–169
 Weinberg, D. H., Burles, S., Croft, R. A. C., et al. 1998, ArXiv Astrophysics e-prints, astro-ph/9810142

Zaldarriaga, M., Hui, L., & Tegmark, M. 2001, Astrophysical Journal, 557, 519
 Zaldarriaga, M., Scoccimarro, R., & Hui, L. 2003, The Astrophysical Journal, 590, 1

APPENDIX

A. THE INFLUENCE OF THE SPECTRAL COVERAGE ON THE RED SIDE OF THE $\text{Ly}\alpha$ EMISSION PEAK

So far we only considered the part of the quasar spectrum on the blue side of the $\text{Ly}\alpha$ emission line, i.e. at shorter wavelengths, where the $\text{Ly}\alpha$ forest is located. However, observed quasar spectra usually cover a much larger wavelength range and extend also to the red side of the $\text{Ly}\alpha$ emission line, i.e. larger wavelengths, where only a few metal lines but no hydrogen absorption interrupt the continua. Therefore this wavelength range might contain information that could improve our estimates of the continuum level in the $\text{Ly}\alpha$ forest region and hence also the constraints on thermal parameters.

There are two questions we would like to address here: how can we use the information on the red side of the quasar spectrum for the fit of the PDF of the transmitted $\text{Ly}\alpha$ flux and the thermal parameter estimation? And how much information about the continuum shape in the $\text{Ly}\alpha$ forest region is contained at wavelengths redwards of the $\text{Ly}\alpha$ line? Therefore we will first introduce a second likelihood function that determines the quasar continuum on the red side of each spectrum. We will then combine this new likelihood function with the previous one from eqn. (13) to form a joint likelihood function and evaluate at the end of this section the impact of adding this information to the estimation of the thermal parameter γ .

A.1. The Likelihood Function for the Continuum on the Red Wavelength Side of the Quasar Spectra $\mathcal{L}_{\text{cont}}$

In § 3.1 we have introduced a likelihood function $\mathcal{L} = \exp(-\chi^2/2)$ (see eqn. (9)) to find estimates for the continuum model to the data that we used to evaluate the intrinsic continuum error of the model. We will now use this likelihood function for the continuum model of each quasar on longer wavelengths than the $\text{Ly}\alpha$ emission line, i.e. on the red side of the spectrum. The likelihood function now reads:

$$\begin{aligned} \mathcal{L}_{\text{cont}} &= \mathcal{L}(\alpha_{ij} | C_{\text{data}}) \\ &= \prod_i^{N_{\text{QSO}}} \prod_{\lambda} \frac{1}{\sqrt{2\pi\sigma_i^2}} \exp\left(-\frac{(C_{\text{model},i\lambda}(\alpha_{ij}) - C_{\text{data},i\lambda})^2}{2\sigma_{i,\text{noise}}^2}\right). \end{aligned} \quad (\text{A1})$$

The free parameters of the continuum model α_{ij} are the coefficients of the PCS j of each quasar i as previously seen in eqn. (8). Thus the likelihood function evaluates how well the continuum model given by eqn. (8) describes the data on the red side of each quasar spectra.

It is important to note that only the wavelength range *redwards* of the $\text{Ly}\alpha$ emission line will be taken into account to evaluate this likelihood function, i.e. 1216Å-1600Å, since there are no absorption lines present (we neglect possible contamination due to metals that are not incorporated into our mock data set — in real data these metals would be straightforward to mask.), whereas the wavelength region *bluewards* of $\text{Ly}\alpha$ will be considered by the previous likelihood function from eqn. (13) as before.

Thus $\mathcal{L}_{\text{cont}}$ takes every pixel at wavelengths on the red side of the quasar spectrum into account, i.e. $\sim 40,000$ data points. This likelihood function is clearly very different in character compared to the previous likelihood function \mathcal{L}_{PDF} (eqn. (13)), where we bin the data and evaluate the difference between the data and the model for every bin in the PDF and thus the likelihood function \mathcal{L}_{PDF} only covers ~ 25 data points. In the next subsection we will combine the two likelihood functions \mathcal{L}_{PDF} and $\mathcal{L}_{\text{cont}}$ and will see, that we have to slightly modify this new likelihood function $\mathcal{L}_{\text{cont}}$ due to its differences in character in order to make the two likelihood functions compatible.

A.2. Combining the Two Likelihood Functions

We would like to join the two likelihood functions $\mathcal{L}_{\text{cont}}$ and \mathcal{L}_{PDF} in order to make use of the information on the continuum level provided by the wavelength coverage on the red side of the $\text{Ly}\alpha$ emission peak, but nevertheless regulate the continuum level via the $\text{Ly}\alpha$ forest flux PDF on the blue side of each quasar spectrum. However, joining these two likelihood functions by multiplication is not as easy as one would naively expect. We have already mentioned that the character of the two likelihood functions is quite different: in one case we evaluate the likelihood for each pixel in the wavelength range between 1216Å-1600Å, i.e. $\sim 40,000$ data points, whereas in the other case we only evaluate the likelihood after binning the pixels, which result in more than three orders of magnitudes less data points. We know that the mean of a χ^2 distribution is roughly equal to the number of degrees of freedom, which corresponds to the number of our data points. Since both likelihood functions are of the shape $\mathcal{L} = \exp(-\chi^2/2)$, this implies that the new likelihood function is much steeper than the other. Hence in a simple multiplication of the two likelihood functions, the steeper function will always dominate the joint likelihood function.

We will therefore modify the new likelihood function $\mathcal{L}_{\text{cont}}$ in order to make the two likelihood functions more compatible. We will augment the function with an additional uncertainty σ_{red} , which reflects the inability of the red

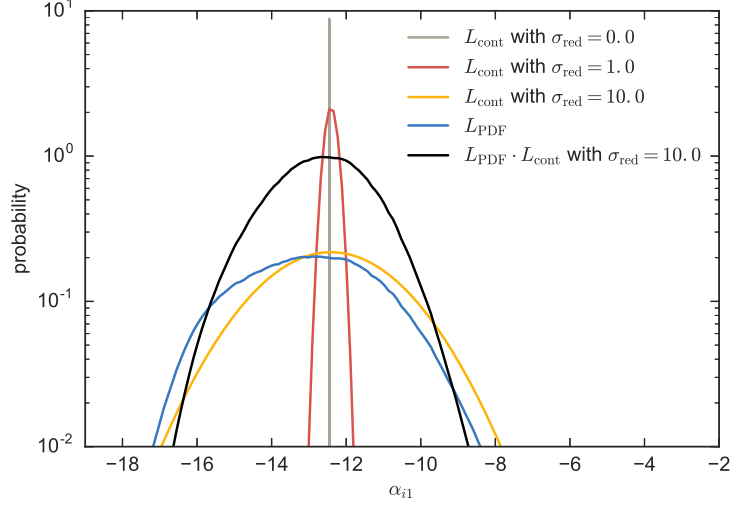


FIG. 13.— Probability distributions given by the likelihood functions $\mathcal{L}_{\text{cont}}$ and \mathcal{L}_{PDF} in dependency of the coefficient α_{i1} of the first principal component spectrum $|\xi_1\rangle$ for an example quasar i at redshift $z = 3$. The gray curve shows $\mathcal{L}_{\text{cont}}$ with no additional variance added to it, i.e. $\sigma_{\text{red}} = 0.0$. By increasing σ_{red} to $\sigma_{\text{red}} = 1.0$ the probability distribution becomes broader and less steep (red curve). For $\sigma_{\text{red}} = 10.0$ shown as the yellow curve the distribution is comparable in its steepness to the probability distribution of \mathcal{L}_{PDF} (blue curve). The black curve shows the joint probability distribution function $\mathcal{L}_{\text{PDF}} \times \mathcal{L}_{\text{cont}}$ with $\sigma_{\text{red}} = 10.0$.

side of each spectrum to predict the continuum on the blue side. Note that this parameter is not one that we estimate with MCMC but rather one that we infer by conducting various tests.

The likelihood function $\mathcal{L}_{\text{cont}}$ then reads:

$$\begin{aligned} \mathcal{L}_{\text{cont}} &= \mathcal{L}(C_{\text{model}}(\alpha_{ij}) | C_{\text{data}}, \sigma_{\text{red}}) \\ &= \prod_i^{N_{\text{QSO}}} \prod_{\lambda} \frac{1}{\sqrt{2\pi\sigma_i^2}} \exp\left(-\frac{(C_{\text{model},i\lambda}(\alpha_{ij}) - C_{\text{data},i\lambda})^2}{2(\sigma_{i,\text{noise}}^2 + \sigma_{\text{red}}^2)}\right). \end{aligned} \quad (\text{A2})$$

Now the two likelihood functions can be joined together by simply multiplying them:

$$\mathcal{L}(\gamma, \sigma_C, \alpha_{ij}) = \mathcal{L}_{\text{cont}}(\alpha_{ij} | \sigma_{\text{red}}) \times \mathcal{L}_{\text{PDF}}(\gamma, \sigma_C, \alpha_{ij}). \quad (\text{A3})$$

The larger the additional error σ_{red} is, the less influence has the likelihood function $\mathcal{L}_{\text{cont}}$ and the more influence has the likelihood function \mathcal{L}_{PDF} in the joint likelihood function. In the extreme case of $\sigma_{\text{red}} \rightarrow \infty$, the likelihood $\mathcal{L}_{\text{cont}}$ would be ignored and we are using only the blue wavelength coverage of each spectrum with \mathcal{L}_{PDF} as we have done in the main text. In the other extreme of $\sigma_{\text{red}} = 0$, we basically fix the continuum level to the best fit of the continuum model to the red side of each quasar spectrum due to the steepness of $\mathcal{L}_{\text{cont}}$ and are not able to regulate the continuum on the blue side via the PDF anymore. The likelihood function \mathcal{L}_{PDF} would then only be used to estimate γ and σ_C with a fixed quasar continuum. A comparison of the two error terms $\sigma_{i,\text{noise}}$ representing the Gaussian white noise that we add to each quasar spectrum with very high S/N-ratio with σ_{red} which reflects the limited ability to predict continuum on the blue side with an estimate of the continuum on the red wavelength side, reveals that the additional error σ_{red} dominates the error budget by roughly 2 – 3 orders of magnitudes.

We illustrate the differences in the steepness of the two likelihood functions in Fig. 13. We show the normalized probability distributions given by the the two different likelihood functions $\mathcal{L}_{\text{cont}}$ and \mathcal{L}_{PDF} dependent on one of the free parameters, the coefficient α_{i1} of the first principal component spectrum $|\xi_1\rangle$ for quasar i at redshift $z = 3$. All other principal component coefficients α_{ij} with $j > 1$ are thereby held fixed. The blue curve shows the likelihood function \mathcal{L}_{PDF} from the Ly α forest PDF, whereas the gray curve represents the likelihood function $\mathcal{L}_{\text{cont}}$ from the continuum emission on the red side of the quasar spectrum with $\sigma_{\text{red}} = 0.0$. The red and yellow curves show also the likelihood function $\mathcal{L}_{\text{cont}}$, but now including an additional error on the red wavelength side σ_{red} . Setting this additional error to $\sigma_{\text{red}} = 1.0$ (red curve) already causes the likelihood $\mathcal{L}_{\text{cont}}$ to flatten and become considerably less steep. Its probability distribution function widens compared to the gray curve with no additional error. Increasing σ_{red} will further flatten the likelihood function and thus increase the width of the probability distribution. This is shown as the yellow curve for $\sigma_{\text{red}} = 10.0$. This new likelihood function results now in a probability distribution function that is of comparable width to the one from the likelihood function \mathcal{L}_{PDF} . Multiplying these two likelihood functions \mathcal{L}_{PDF} and $\mathcal{L}_{\text{cont}}$ with $\sigma_{\text{red}} = 10.0$ results in the probability distribution shown in black.

Note that the true value for this parameter for this particular quasar is $\alpha_{i1} \approx -11.4$, which is strongly disfavored by fitting the pixels redward of the Ly α line if the σ_{red} is too small.

A.3. Results Including the Red Wavelength Side of the Quasar Spectra

In Fig. 14 we show the results of our analysis when including the information of each quasar spectrum redwards of the Ly α emission line. We show the same quantities as in the previous Fig. 12 for $z = 3$ and $z = 5$ in the left and right panels, respectively. The upper panels show the distribution of medians of a hundred posterior probability distributions of γ estimated from different realizations of an ensemble of ten quasar spectra. The middle panels show the distribution of medians of the continuum residual $\Delta C/C$ distributions of each run, and the lower panels depict the continuum error — once measured as the widths of each continuum residual distribution, i.e. the actual PDF regulated continuum error $\sigma_{\Delta C/C}$, shown as the blue data points and once inferred via MCMC as a free parameter influencing the shape of the PDF, i.e. the estimated continuum error σ_C . In this case the medians of the posterior probability distributions are used again as the best estimate. The medians and 68%-regions of this distributions of best estimates are shown as the black data points.

However, the x-axis of Fig. 14 now shows the additional error σ_{red} that was added to the new likelihood function $\mathcal{L}_{\text{cont}}$. A value of $\sigma_{\text{red}} \rightarrow \infty$ indicates that the likelihood $\mathcal{L}_{\text{cont}}$ and thus the red side of each quasar spectrum has no influence in the joint likelihood function and only the spectral coverage bluewards of the Ly α emission line is used to regulate the quasar continuum. This is the case we have discussed extensively in § 4.2. Decreasing values of σ_{red} increase the influence of $\mathcal{L}_{\text{cont}}$ in the joint likelihood function. We run our algorithm as before a hundred times with different realizations of an ensemble of ten quasar spectra in order to avoid statistical fluctuations due to the limited number of quasar spectra. Throughout this analysis we work with a continuum model with two PCS, i.e. $N_{\text{PCA}} = 2$. The gray and blue shaded areas in all panels depict the same ideal cases as in Fig. 12, i.e. the gray shaded areas in the upper panels show the precision on γ achievable when assuming noise-free spectra and perfectly known quasar continua and the blue shaded areas in the middle and lower panels illustrate the intrinsic uncertainty of the chosen continuum model.

The behavior of our algorithm at $z = 3$ and $z = 5$ is similar. Surprisingly, the additional information of the wavelength coverage on the red side of each quasar spectrum does not seem to improve the estimation of the thermal parameter γ significantly. The opposite even seems to be the case at $z = 3$ for values of σ_{red} that are too small, i.e. $\sigma_{\text{red}} = 1.0$, where the 68%-region is significantly larger than for higher values of σ_{red} . However, the additional information on the red wavelength side does improve the quasar continuum estimation and reduces the small bias in the medians of the continuum flux residual distributions (middle panels) from $\mu_{\Delta C/C} \approx -1.5\%$ to $\mu_{\Delta C/C} \approx 0.2\%$ at $z = 3$ and from $\mu_{\Delta C/C} \approx -2.3\%$ to $\mu_{\Delta C/C} \approx 0.3\%$ at $z = 5$ for $\sigma_{\text{red}} = 10.0$ compared to the previous case from § 4.2 when only wavelengths bluer than Ly α , i.e. $\sigma_{\text{red}} \rightarrow \infty$, were taken into account.

The inferred estimates for the continuum error σ_C (lower panels) also reflect this improvement in the quasar continuum model for $\sigma_{\text{red}} = 10.0$. At $z = 3$ the measured (blue data point) and inferred (black data point) estimates for the continuum error agree perfectly and show that our algorithm results in a reliable estimate of the actual continuum error. For lower values of σ_{red} the continuum level estimation is set entirely by the very steep red side continuum likelihood, which causes the continuum model on the blue wavelength side to not be a good fit anymore. Hence the 68%-region of the estimates for the continuum error increases in the actual PDF regulated continuum error $\sigma_{\Delta C/C}$ as well as in the inferred values for σ_C . We mentioned already that the agreement of the measured and estimated continuum errors at $z = 5$ is probably only coincidental and reflects our choice of prior assumptions, since we do not have good constraints on σ_C at these redshifts from the Ly α flux PDF.

We conclude that the information of the spectral coverage on the red wavelength side of each quasar spectrum does contain information for improving the quasar continuum model on the blue wavelength side of each spectrum. However, it is necessary to introduce an additional error σ_{red} in order to prevent the likelihood function $\mathcal{L}_{\text{cont}}$ to over-regulate the continuum model on the red side of the quasar spectrum. We experimentally determined the best value to be $\sigma_{\text{red}} \approx 10.0$, i.e. we add an error that enlarges the noise on the red wavelength side of each quasars by multiple orders of magnitudes compared to the Gaussian noise that was added to the spectra. Note that this choice for σ_{red} is purely based on the intent to match the widths of $\mathcal{L}_{\text{cont}}$ to \mathcal{L}_{PDF} , i.e. there is no physical meaning to its specific value.

However, the additional information of the red spectral coverage, does *not* improve the estimation of the thermal parameter γ , regardless of the exact choice for the value of σ_{red} . Since the computational time increases significantly when adding the likelihood $\mathcal{L}_{\text{cont}}$, we advocate using it only when interested in the continuum estimation of the quasars. If the thermal parameters are the main parameters of interest, $\mathcal{L}_{\text{cont}}$ provides no additional information and the computational time will be significantly shorter without including the red side likelihood function.

B. JUSTIFICATION OF OUR ANALYTICAL MODEL FOR THE LY α FOREST

B.1. Comparison to Hydrodynamical Simulations

This study considered a highly simplified analytical model to simulate the Ly α forest absorption in high redshift quasars. We will show now that the flux PDF of our analytical model behaves qualitatively similar to the PDF from hydrodynamical simulations. Therefore we choose different runs from the NyX simulations (Almgren et al. 2013), that differ in the slope parameter γ of the temperature-density relations, but other thermal parameters such as the temperature at mean density or the Jeans smoothing scale are kept fixed. The parameters of the chosen NyX simulations coming closest to our requirements had $\gamma = 1.011$ ($T_0 = 10892$ K, $\lambda_P = 64.5$ ckpc) and $\gamma = 1.575$ ($T_0 = 10753$ K, $\lambda_P = 66.5$ ckpc) at $z = 3$, and $\gamma = 0.9436$ ($T_0 = 7500$ K, $\lambda_P = 69.66$ ckpc) and $\gamma = 1.5219$ ($T_0 = 7713$ K, $\lambda_P = 67.4$ ckpc) at $z = 5$. Thus we compare these simulations to the PDF from the analytical models

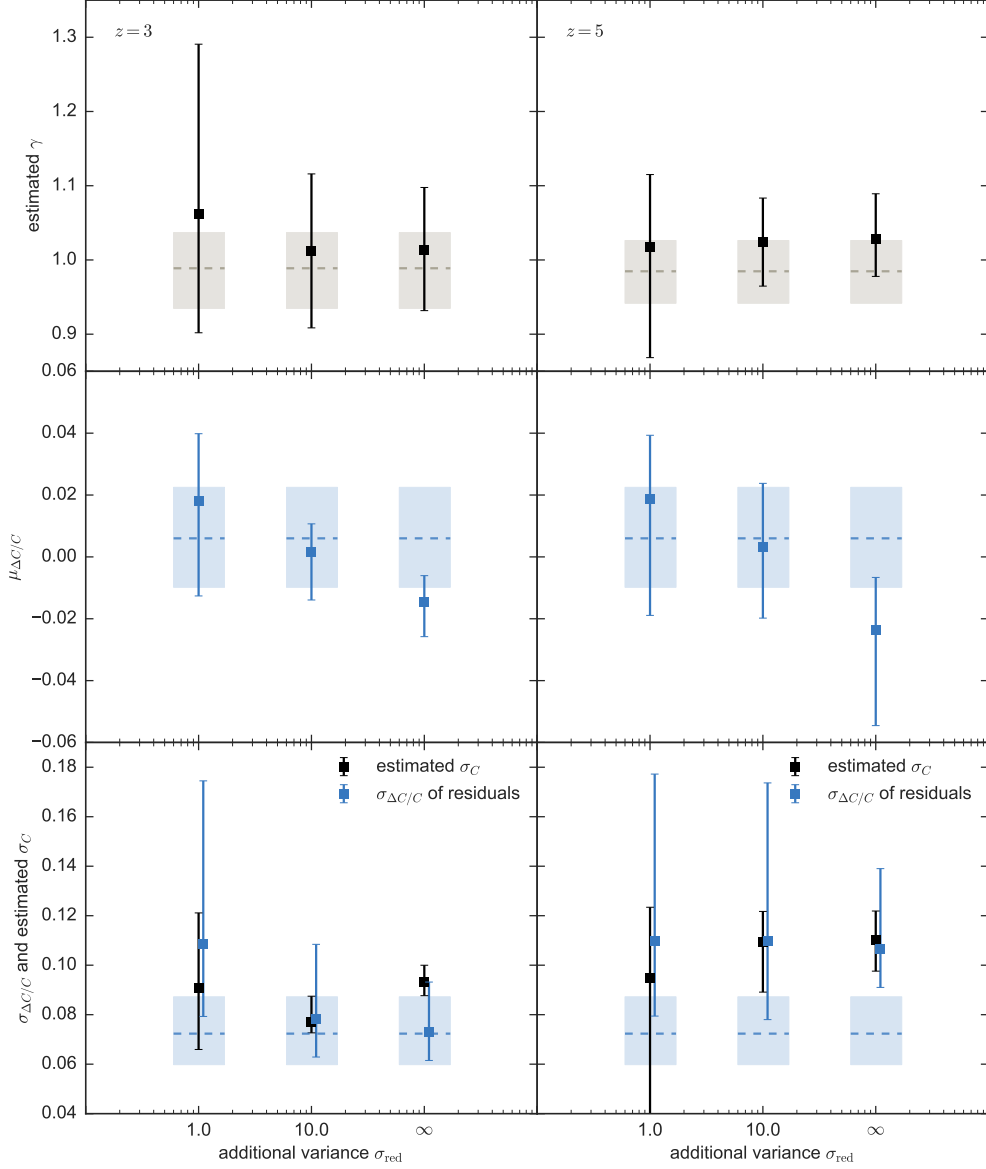


FIG. 14.— Results of the analysis of the impact of the red wavelength side of each quasar continuum. The x-axis shows the additional error σ_{red} added to the spectra on wavelengths larger than $\text{Ly}\alpha$ in order to make the two likelihood functions compatible. The upper panels show the median and 68%-region of estimates for γ . The gray areas indicate the precision achievable when estimating γ for ensembles of noise-free quasar spectra and perfectly known quasar continua. The middle panels show the median and 68%-region of median values of the continuum flux residuals distributions in the $\text{Ly}\alpha$ forest region. The blue shaded areas indicate the intrinsic precision of the chosen continuum model with $N_{\text{PCA}} = 2$. The lower panels show the uncertainty of the continuum estimation. The black data points show the median and 68%-region of estimates for the continuum error σ_C , whereas the blue data points show the actual measured values of the 16th and 84th percentiles of the continuum flux residuals, i.e. the actual PDF regulated continuum error $\sigma_{\Delta C/C}$. The blue shaded areas show again the intrinsic uncertainty of the chosen continuum model.

with $\gamma = 1.01$ and $\gamma = 1.58$ at $z = 3$, and $\gamma = 0.94$ and $\gamma = 1.52$ at $z = 5$. We calculate the difference in the PDF models for our analytical model and the hydrodynamical simulations and plot the relative change

$$\frac{\Delta \text{PDF}}{\text{PDF}} = \frac{\text{PDF}(\gamma = 1.58) - \text{PDF}(\gamma = 1.01)}{\text{PDF}(\gamma = 1.01)}, \quad (\text{B1})$$

for $z = 3$ in the left panel of Fig. 15, and correspondingly for $z = 5$ in the right panel. The PDF from hydrodynamical simulations differs from the analytical model on a 10–20% level, but shows qualitatively the same behaviour. Choosing a different smoothing kernel in our analytical model could reduce these differences (see § B.2), i.e. the analytical model with slightly higher smoothing kernel will resemble more closely the PDF from the NyX simulations. Thus we do not expect any discrepancies arising in the parameter estimation with our new method due to the the simplified analytical model with which the PDF models are constructed.

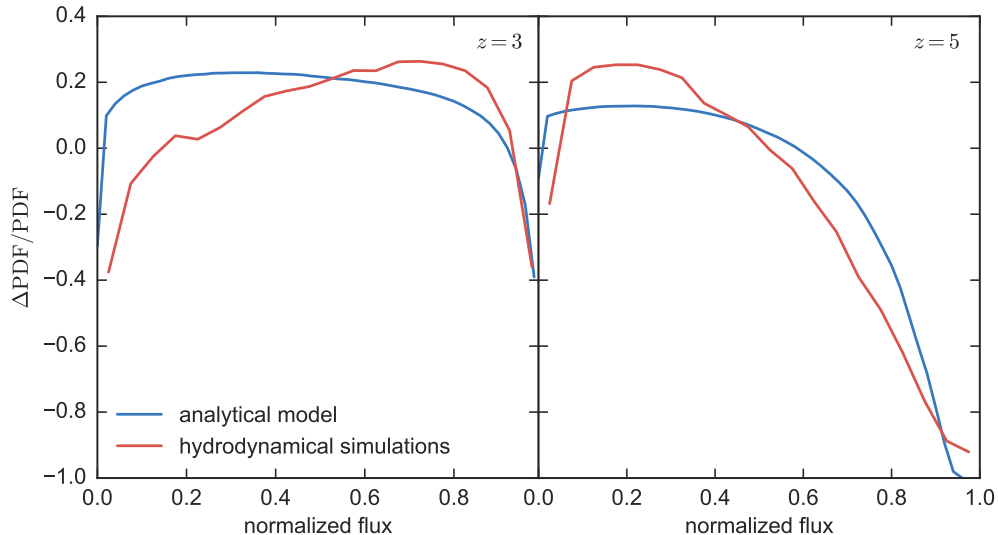


FIG. 15.— Comparison between the flux PDF's from the analytical model for the Ly α forest (blue curves) and from NyX hydrodynamical simulations (red curves) for $z = 3$ and $z = 5$ in the left and right panel, respectively. The y-axis is showing the relative change between a PDF models from eqn. B1

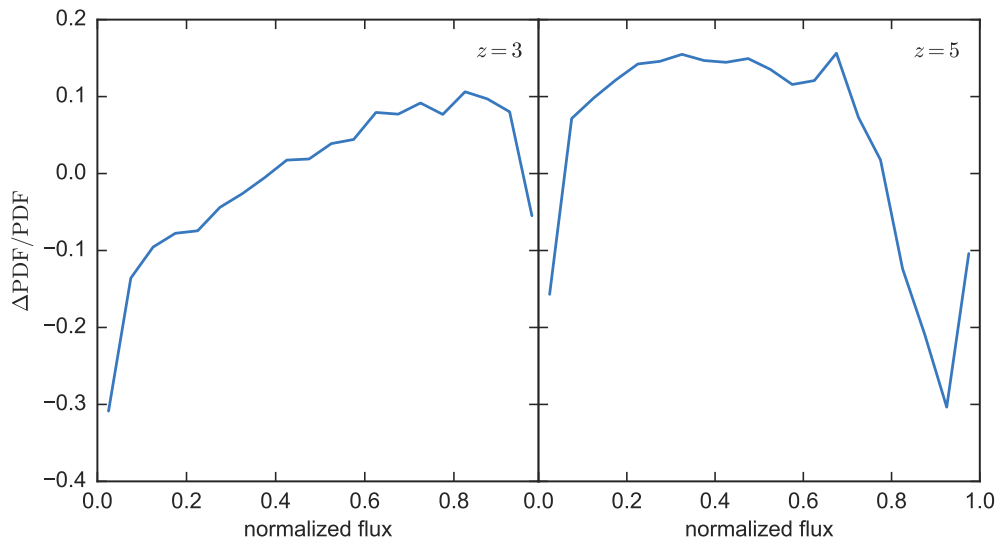


FIG. 16.— Relative difference between two PDF models with smoothing kernels $\sigma_\tau = 20 \text{ km s}^{-1}$ and $\sigma_\tau \approx 28 \text{ km s}^{-1}$ for $z = 3$ and $z = 5$ in the left and right panel, respectively.

B.2. Smoothing Kernel Applied to the Density Field

In order to test the influence of the smoothing kernel σ_τ that has been applied to the density field (see § 2.1) we show in Fig. 16 the relative differences between two PDF models with a smoothing kernel $\sigma_\tau = 20 \text{ km s}^{-1}$ and a smoothing kernel of $\sigma_\tau \approx 28 \text{ km s}^{-1}$, which roughly corresponds to a change in temperature of a factor of two, i.e. $\Delta T \approx 0.3 \text{ dex}$. We plot

$$\frac{\Delta \text{PDF}}{\text{PDF}} = \frac{\text{PDF}(\sigma_\tau \approx 20 \text{ km s}^{-1}) - \text{PDF}(\sigma_\tau \approx 28 \text{ km s}^{-1})}{\text{PDF}(\sigma_\tau \approx 20 \text{ km s}^{-1})}. \quad (\text{B2})$$

Changing the smoothing kernel influences the shape of the PDF on a 10% level, however, the slope parameter γ has a significantly stronger influence on its shape. In the future, the smoothing kernel σ_τ could be easily incorporated into our PDF models and be treated as a nuisance parameter.